Chapter 5
Thin-Film Photovoltaic Devices Based on A^2B^6 Compounds

Tamara Potlog

Abstract This review gives a brief description of four types of photovoltaic devices based on A_2B_6 thin film semiconductors. Among A_2B_6 semiconductors CdTe is widely researched due to its near ideal band gap energy of 1.45 eV for the achievement of the theoretical maximum photovoltaic conversion efficiency of 31 %. The first part of the paper highlights the history of CdS/CdTe thin-film photovoltaic devices. It also describes the basic physics and design of CdS/CdTe and ZnSe/CdTe thin film heterojunction photovoltaic devices prepared by close spaced sublimation method at Moldova State University. The second part of this paper discusses the physical properties of novel TiO_2 oxide as a partner in heterojunction with CdSe and CdTe thin films. This section also describes the physics, design, and fabrication process of thin film photovoltaic devices based on TiO_2/CdSe and TiO_2/CdTe structures.

5.1 Introduction

The highest efficiency of conversion of solar light into electricity has been demonstrated in photovoltaic devices made from single-crystal semiconductor wafers. Traditional single-crystal solar cells, such as Si and GaAs [1–5], demonstrate very high efficiencies (20–30 %), but the production is expensive. Thin film solar cell technology offer the best hope for obtaining photovoltaic devices with low price and reasonable efficiency. Thin-film crystalline-silicon (c-Si) solar cells are considered to be one of the most promising alternatives to bulk silicon solar cells [6]. Thin films significantly decrease the silicon wafer cost, which accounts for about half of the total cost of standard silicon solar modules. Thin-films

T. Potlog (✉)
Department of Physics and Engineering, Moldova State University, Chisinau, Moldova
e-mail: tpotlog@gmail.com

© Springer International Publishing Switzerland 2016

I. Tiginyanu et al. (eds.), *Nanostructures and Thin Films for Multifunctional Applications*, NanoScience and Technology,
DOI 10.1007/978-3-319-30198-3_5

crystalline-silicon (c-Si) solar cells are made a few μm thick, as opposed to at least several hundred μm for most Si wafers. Since such little amount of semiconductor is used, material cost is greatly reduced with respect to crystal substrate cells, making even relatively low efficiency thin-film solar panels cost-competitive with Si modules. Today crystalline silicon (c-Si) still accounts for 85 % of the market though the cost of manufacturing remains higher. Recently, Morales-Vilches, A. group has obtained a remarkable conversion efficiency of 17.2 % on 1 cm^2 hydrogenated amorphous silicon (a-Si:H) layers deposited at low temperature on crystalline silicon (c-Si) substrates [7, 8]. Amorphous silicon shows long term-stability issues. Significant thin-film PV production levels are also being set up for CdTe [9] and copper-indium-gallium-di-selenide (CIGS) [10]. CIGS requires expensive elements such as indium, gallium, and careful proportioning of the component elements. Representative examples of high-efficiency A_2B_6 thin films PV devices are the *n*-CdS/*p*-CdTe heterojunction [11]. These PV devices feature many of the technologies that provide high efficiency in this type of PV cell. Cadmium telluride has been identified as the principal candidate for low cost thin film photovoltaic applications because of the direct band gap and the ability to be doped both *n*-and *p*-type, allowing the formation of a variety of junction structures. The CdTe thin film photovoltaic devices have shown long-term stable performance [12] and high efficiency under AM1.5 illumination for terrestrial application. In many respects, CdTe resembles CIGS solar cells and can be produced with similar techniques, though much easier.

The main purpose of this overview is to demonstrate the possibility to manufacture other types of A_2B_6 photovoltaic devices based on CdTe with high efficiency in order to form multijunctions to push efficiencies beyond the Schockley-Queisser limit for single band-gap PV devices. This review will give a brief general discussion on the characterization of the ZnSe/SnO_2 interface. Then, the review will continue with the characterization of the ZnSe/CdTe photovoltaic devices and the comparison with the CdS/CdTe devices fabricated at Moldova State University. Finally, a brief description on *n*-TiO_2 nanostructured thin films for photovoltaic applications and a characterization of the TiO_2/CdTe, TiO_2/CdSe photovoltaic devices will be given.

5.2 Historical Development of the CdS/CdTe Photovoltaic Devices

Research in CdTe began in the 1950s and Loferski [13] first proposed the CdTe PV technology. CdTe with a band gap of 1.45 eV (300 K), high absorption coefficient ($\sim 10^5$ cm^{-1}) and a high chemical stability perfectly matched to the distribution of photons in the solar spectrum in terms of optimal conversion to electricity.

The most commonly used CdTe thin film photovoltaic devices are the *p-n*-heterojunction devices. Standard CdTe-based photovoltaic devices employ a “superstrate” and “substrate” designs. In the “superstrate” design, sunlight enters through the transparent substrate, which is usually glass or a transparent plastic. The insulating substrate needs a conducting layer, which is typically a “transparent conductive oxide” (TCO) such as SnO_2. The p-n-heterojunction is fabricated by the successive deposition of the *n*-type window layer (CdS), the *p*-type CdTe absorber, and finally the back metal contact is applied. Superstrate design of the device was first demonstrated in 1969 by Adirovich et al. with an efficiency >1 % with evaporated CdTe on a CdS/SnO_2/glass substrate [14]. In the “substrate” configuration, sunlight enters the p-n heterojunction before it reaches the substrate. Starting with the substrate, the cell is fabricated in the reverse order compared to the superstrate design: first a back contact, then the p-n heterojunction layers (starting with an n-type layer), and finally a TCO layer to act as an electrode to the window layer of the p-n HJ. In 1972 Bonnet and Rabenhorst [15] first proposed CdTe/CdS thin-film photovoltaic device in the “substrate” configuration. They reached 5–6 % efficiency in the substrate design of CdS/CdTe/Mo made by chemical vapor–deposited CdTe and vacuum-evaporated CdS thin films. These two configurations permit a very wide range of applications for CdTe photovoltaic devices. The “superstrate” design can be integrated as architectural element in buildings. The “substrate” configuration has been developed using stainless steel substrates. Attempts were made to develop CdTe/CdS solar cells in a “substrate” configuration with efficiencies in the range 3.5–8 % by Enrıquez et al. in 2004 on metal foils [16], Matulionis et al. [17], Vijay et al. [18], Mathew et al. [19]. One of the obstacles in the development of CdTe devices on metallic substrates is that most of the metal foils do not form an efficient ohmic contact with CdTe and it is difficult to incorporate an additional buffer layer as ohmic contact to increase the cell efficiency. The criteria of matching thermal expansion coefficients and work function, limit the choice of available substrate materials. The progress in R&D got real impulse, in 1980s when Tyan and Perez-Albuerne reported CdTe/CdS thin film solar cells with efficiency of 10 % [20]. In 1980s the various techniques were developed, such as electro deposition (ED), screen printing, vacuum evaporation and close spaced sublimation (CSS) method. The efficiencies exceeding 10 % were achieved for CdTe/CdS heterojunction solar cells by Basol [21], by Chu [22], by Mitchell et al. [23]. The pioneering work of different groups in the 1990s pushed the efficiency to above 15 %. Ferekides et al. reported increased efficiency of 15.8 % [24]. Finally, Wu et al. reported a record efficiency of 16.5 % by modifying the conventional structure (SnO_2/CdS/CdTe/metal) with CTO/ZTO/CdS/CdTe/Cu:HgTe:Cu_xTe) structure.

5.3 Technology Development Trends by Companies in CdS/CdTe Photovoltaic Market

Early leaders in CdS/CdTe device efficiencies were General Electric in the 1960s [26] and then First Solar (USA, vapor transport) [27], British Petroleum Solar (UK, electro-deposition) [28], Matsushita (Japan, screen printing and close space sublimation) [29] and Antec (Germany, close space sublimation) [30]. In the early 2000s BP Solar finally realized that electrodeposition is too slow for large scale production and exited thin-film technology. Antec has bankrupted and was bought by a wind-turbine company, but lost its key scientific personnel. Matsushita claimed an 11 % module efficiency using CSS and then dropped out of the technology, perhaps due to internal corporate pressures over cadmium which is highly toxic and closed down their CdTe program. At present, only First Solar (USA) remains in the field [31]. The company First Solar Inc. dominates not only the production of thin film solar modules but the whole PV market in terms of large production volume and lowest cost of production. Besides First Solar, today, there are a number of start-ups in CdTe: Q-Cells' Calyxo (Germany), GE's PrimeStar Solar (Arvada, Colorado), Arendi (Italy), and Abound Solar (Fort Collins, Colorado). The progress of conversion efficiency in CdS/CdTe photovoltaic devices was reported by First Solar (FSLR) [31] and summarized in Table 5.1.

The data are reproductions from references [32–35]. Development of thin-film CdS/CdTe photovoltaic device fabrication processes was advanced by the application of a cadmium stannate transparent conductive oxide layer in superstrate design. This allowed NREL researchers [31] to increase efficiency to 16.7 %. This world record efficiency happened to be the record from 2001 through 2011. After stagnation over a long period, First Solar (FSLR) announced in 2011 an efficiency of 17.3 %. However, quickly First Solar has lost the lead in cell efficiency as the General Electric (GE) Research Firm Announced efficiency of 18.3 % in 2012 year. CdTe solar-cell efficiency has been rapidly increasing since FSLR fabricated an

Table 5.1 CdTe record cell photovoltaic parameters

Year	Team	Efficiency (%)	V_{oc} (V)	J_{sc} (mA/cm^2)	FF (%)	References
1993	USF[a]	15.8	843	25.1	74.5	[3]
1997	Matsushita[b]	16.0	840	26.1	73.1	[5]
2001	NREL[a]	16.4	848	25.9	74.5	[6]
2001	NREL[a]	16.7	845	26.1	75.5	[4]
2011	FSLR[a]	17.3	845	27.0	75.8	[7]
2012	GE[a]	18.3	857	27.0	79.0	[8]
2012	FSLR[a]	18.7	852	28.6	76.7	
	Demtsu/sites-target	19.0	900	27.0	78.5	[1]

[a]NREL certified
[b]JQA certified

18.7 % NREL certified cell at the end of 2012. Today, GE and FSLR announced a technology partnership to advance thin-film photovoltaic devices and modules. In 2013 First Solar has acquired GE's global CdTe solar intellectual property portfolio, setting a course for significant advancement of photovoltaic thin-film solar technology and announced an efficiency of 18.7 % on the cell. Through optimized processing of the CdTe thin film, the quality of the grain boundaries, doping and contacting Demtsu and Sites in their paper [36] proposed an achievable performance target for CdTe solar cells of 19 %. The Target cell is one that should be possible with current industrial processes. The current-voltage parameters were predicted to reach 900 mV open-circuit voltage, 27 mA/cm^2 short-circuit current density and 77 % fill-factor. The analysis concludes that further optimization of the cell and module design beyond the present, allows increasing cell efficiency to17–18 % without disruptive technology changes at the module level at FSLR.

5.4 Comparison of Moldova State University CdS/CdTe Photovoltaic Device with Manufacturing Target

Research in the development of CdS/CdTe photovoltaic devices fabricated by close spaced sublimation method occurs at Physics Department and Engineering of Moldova State University (MSU). Gashin and coworkers [37] fabricated the first CdS/CdTe thin film photovoltaic devices in 1984. A few years later, Potlog et al. published in the paper [38] an efficiency of about 9 %. Additional of Te layer before the metallic back contact has improved MSU CdS/CdTe solar-cell efficiency and today the MSU researchers achieved 10.5 % NREL certified cell. The NREL I-U curves of the certified 10.5 % MSU and FSLR, USA 18.7 % best devices are shown in Fig. 5.1. As one can see, the primary improvement in the MSU cell should be addressed to the fill-factor. Figure 5.2 compares the quantum efficiencies of the MSU device with the world record cell. The primary loss over this range is the reflection of the cell. Also, the loss that needs to be addressed occurs for short wavelengths, as can be seen.

5.5 Deposition Processing and Photovoltaic Device Fabrication

The close spaced sublimation (CSS) method is considered one of the most promising techniques for A_2B_6 thin films deposition. The CSS method allows growing high-quality semiconductor thin films under a controllable technological process. It should be noted that the CSS method allows one to obtain thin films under close to thermodynamically equilibrium growth conditions at high substrate

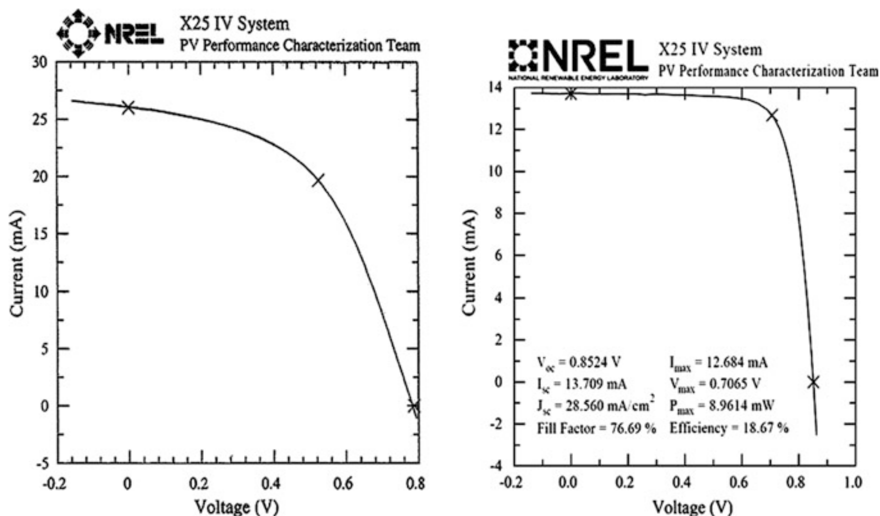

Fig. 5.1 NREL certified current-votage curves of the 10.5 % MSU and the 18.7 % FSLR photovoltaic devices

Fig. 5.2 Quantum-efficiency comparison of highest-efficiency MSU photovoltaic device with manufacturing target

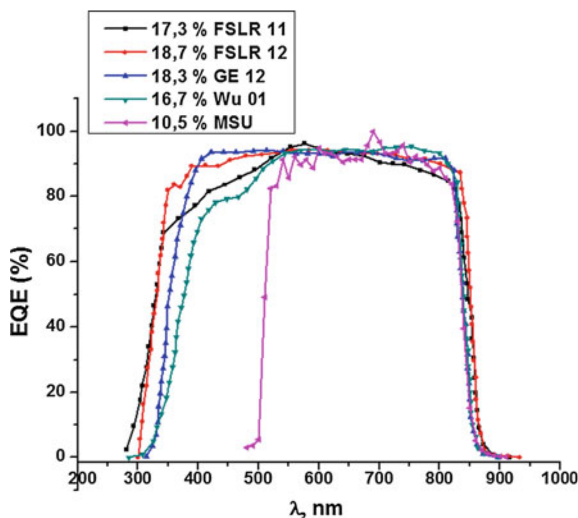

temperature T_s and a small difference between substrate temperature and evaporation temperature ΔT ($\Delta T = T_e - T_s$) [39]. In our study, a source and a substrate separated by a 20 mm distance are introduced in a controlled vacuum atmosphere, and the source is maintained at a higher temperature than the substrate. The A_2B_6 source material dissociates into its A atoms and B_2 molecules which collide several times with gas molecules and then condense on the substrate surface. This process

provides direct transport of each component of the source across the space to the substrate, and in most cases, the transport mechanism is diffusion-limited. The polycrystalline CdS, ZnSe, CdTe and CdSe thin films were obtained in a short time (about 30 min) without an additional transport agent gas. The MSU CdTe heterojunction photovoltaic devices are grown in "superstrate" design. The most suitable window electrode material is the tin oxide doped by fluorine (SnO_2:F). The low-cost soda-lime glass substrates covered with SnO_2:F for a processing at temperature below 500 °C we purchased from Solaronix, Swiss. The SnO_2/glass slides with a size of 20 mm × 20 mm were washed with detergent and rinsed with deionized water followed by rinsing in methanol. SnO_2: F layer with an electron affinity below 4.5 eV forms an ohmic contact and has good band alignment with *n*-CdS and *n*-ZnSe. The ZnSe, CdS and CdTe thin films were deposited on glass substrate covered with TCO at a system pressure of $\sim 10^{-6}$ Torr. The as-deposited CdS/CdTe and ZnSe/CdTe photovoltaic devices exhibit poor PV properties and thus require a special annealing treatment that improves the device efficiency considerably. This is done by subjecting the CdS/CdTe and ZnSe/CdTe stacks to a heat treatment under $CdCl_2$ atmosphere. After this annealing treatment, a significant enlargement of grain size is observed in CdTe grown at temperatures below 500 °C. Another important issue in CdTe photovoltaic device technology is the formation of an efficient and stable ohmic contact on the *p*-CdTe layer. For forming on a *p*-type semiconductor of an ohmic contact, the work function of the metal should be higher than that of the semiconductor; otherwise, a Schottky contact is formed. For the *p*-CdTe layer, a metal with a work function higher than 5.7 eV is needed. Metals with such high work functions are not available. To overcome this problem, a heavily doped *p*-CdTe was created by deposition of Te on the surface by thermal evaporation. Ni or Cr is used as an ohmic metal contact for *p*-CdTe by thermal evaporation.

TiO_2 thin films were prepared on glass substrates by radio frequency RF magnetron sputtering of Ti target of 99.99 % purity by researchers from Al.I. Cuza University, Iasi, Romania. TiO_2 thin films doped with oxide powder Nb_2O_5 of 99.999 % purity were prepared. The sputtering was performed under a mixture of 5 sccm (standard cubic centimeters per minute) of Ar (99.99 %) and 1 sccm of O_2 (99.99 %) atmosphere supplied as working and reactive gases, respectively, through an independent mass-flow controller. The sputtering chamber was evacuated down to 1×10^{-5} mbar by the turbo molecular pump and the working pressure was kept at about 5×10^{-3} mbar. During the depositions, the RF power was 100 W and the substrates were kept at room temperature using the same deposition time of 8 h. The distance between the target and the substrate was kept constant at 6 cm. Before the deposition, the glass substrates were sequentially cleaned in an ultrasonic bath with acetone and ethanol. Finally, the substrates were rinsed with distilled water and dried. After the deposition, TiO_2 films were vacuum annealed at 420 °C for 30 min in the deposition chamber at a pressure of 4.0×10^{-5} mbar and in hydrogen atmosphere at a pressure of 2.0×10^{-3} mbar at the same temperature and duration.

The TiO_2/CdTe and TiO_2/CdSe photovoltaic devices were fabricated by CdTe and CdSe layers deposition on the Nb-doped TiO_2/glass substrates by close space sublimation method.

5.6 Analysis of Efficiency Loss Mechanism in MSU CdS/CdTe Photovoltaic Devices

5.6.1 Current-Voltage Characteristics of the CdS/CdTe Photovoltaic Devices

Two types of the CdS/CdTe photovoltaic devices fabricated by close space sublimation (CSS) [40] and high vacuum evaporation (HVE) [41] are compared here. Both types were fabricated in "superstrate" design (Fig. 5.3). In the case of devices fabricated by CSS the structures were held in either $CdCl_2$:H_2O saturated solutions and then annealed in the air at 400 °C for 25–30 min. $CdCl_2$ treatment for the cells made by HVE is applied by evaporating 400–600 nm onto the CdTe surface and then annealing them in the air at 430 °C for 30 min. Back contact in the case of CdS/CdTe fabricated by CSS was made by evaporating Te/Ni, but in the case of those fabricated by HVE–Cu/Au, followed in both cases by a short annealing at 200 °C in the air.

Photovoltaic devices are designed to work under normal sunlight and their performances are evaluated at 25 °C under an AM1.5 solar irradiation of 100 mW/cm^2 intensity through the CdS thin film. Figure 5.4 shows current-voltage characteristics of CdS/CdTe photovoltaic devices made by (HVE) and CSS methods.

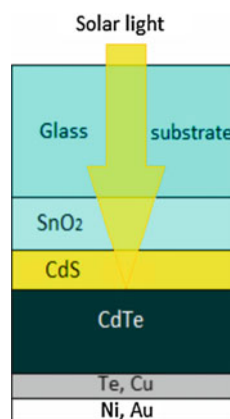

Fig. 5.3 Schematic structure of the CdS/CdTe thin film photovoltaic device

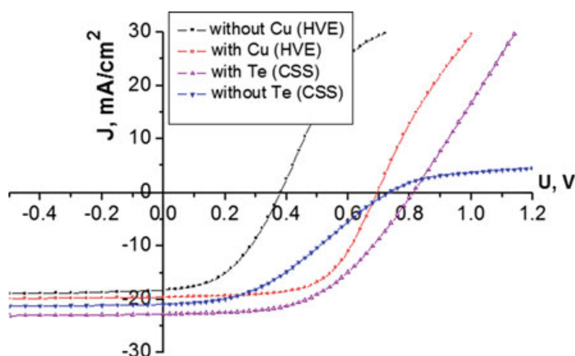

Fig. 5.4 Current-voltage characteristics of the CdS/CdTe photovoltaic devices fabricated by different methods of deposition at illumination of 100 mW/cm^2

The data can be fitted to the usual expression, which includes the effect of series and shunt resistances:

$$J = J_0\left[\exp q\frac{(U - JR_s)}{AkT} - 1\right] + q\frac{(U - JR_s)}{R_{sh}} \tag{5.1}$$

where J_0 is the reverse saturation current density, A is the diode ideality factor, R_s the series resistance and R_{sh} the shunt resistance, k is Boltzmann constant and T is the temperature. R_{sh}, R_s, n, J_0 are cell parameters of the device. The series resistance in the dark is appreciable for all cells but decreases to about 6–7 Ω cm^2 under 100 mW/cm^2 illuminations. This is due to the high photoconductivity of CdS and CdTe thin films. The J-U curve for the cell without the Te layer shows a stronger rollover in the light in forward bias than the cell without Cu. The addition of small amounts of Cu or Te to back contacts improves contact properties by p^+-doping the CdTe surface and creating a pseudo-ohmic contact. The cell made by close spaced sublimation method shows the highest open circuit voltage. The short circuit current is high enough for both cells. The cell deposited by CSS seriously suffers in *FF* compared to the cells fabricated by HVE. It's well known the FF is a function of the series/shunt resistance

$$FF = FF_0\left(1 - \frac{R_s}{R_{sh}}\right). \tag{5.2}$$

FF_o—the fill factor which is not affected by the series resistance. From Table 5.2 we can observe that R_s for CdS/CdTe with Te is five times higher than for cells with

Table 5.2 Photovoltaic parameters of CdS/CdTe photovoltaic devices fabricated by HVE and CSS methods

Cell	J_{sc} (mA/cm^2)	U_{oc} (V)	FF (%)	η (%)	R_s (Ω cm^2)	R_{sh} (Ω cm^2)
Without Cu (HVE)	18.21	0.38	45.3	3.14	43.54	2003.8
With Cu (HVE)	21.42	0.65	60.8	8.47	2.01	538.6
Without Te (CSS)	20.91	0.7317	38.67	5.92	24.71	3310.5
With Te (CSS)	22.75	0.81	51.87	9.56	10.68	2917.4

Cu. This is due probably to the fact that the cell prepared by CSS used wet $CdCl_2$ treatment and may contain oxide on the surface, while cells with Cu used evaporated $CdCl_2$. There is a big difference between the value of U_{oc} in the case of cells prepared by HVE and CSS. It is well known that a cell containing a back barrier can operate in either standard: back-diode or reach-through diode regime. In order to confirm this fact the device parameters have been plotted against the intensity of illumination (*E*). The U_{oc} = f(E) dependence for devices prepared with Cu and without Cu at the back contact (Fig. 5.5) is independent of the intensity of illumination. The back barrier of these devices operates in reach-through diode regime. In the case of the cell without Te the back barrier operates as a back diode and it's considered as a good back contact. The addition of a Te layer diminishes the back barrier and the J-U curve shows a normal behavior. The U_{oc} for both cells fabricated by CSS method increases, and then tends to saturation with illumination. According to the theory, the total cell efficiency depends on the properties of the back contact only through the fill factor. The series resistance and the dark J-U characteristics determine the fill factor. The main source of the *FF* decrease is an increase in J_o. To a second approximation the diode factor *A* value can influence the *FF*, if R_s becomes high enough, even though an increase in R_s itself is much more important than enhanced *A*. Such a behaviour of the *FF* of CdS/CdTe photovoltaic devices with and without Te (Fig. 5.6) is explained by the high value of R_s, which changes with illumination (Fig. 5.7).

In contrast to our expectations, the highest value of η = 9.5 % for a CdS/CdTe (Fig. 5.8) solar cell with Te was obtained not for the highest illumination intensity of 100 mW/cm^2, but for 50 mW/cm^2. For the cells without Te the highest value of η was obtained for the lowest light intensities in the range of 30 mW/cm^2. For the cells with Cu the highest value η = 8.47 % was obtained for the highest intensity of 100 mW/cm^2, that is why the intensity R_s is smaller. As was mentioned above, the *FF* depends on both R_s and R_{sh} in a complex way. The most dramatic is the variation of R_{sh} in both cases of fabrication of the devices with a light intensity (see Fig. 5.7).

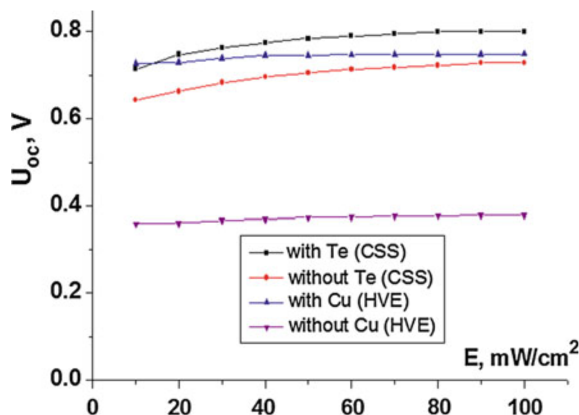

Fig. 5.5 The dependence U_{oc} = f(E) for CdS/CdTe devices fabricated by different methods of deposition

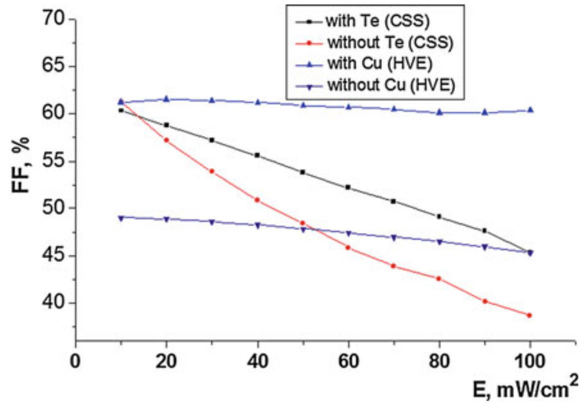

Fig. 5.6 The dependence FF = f(E) for CdS/CdTe solar cells fabricated by different methods of deposition

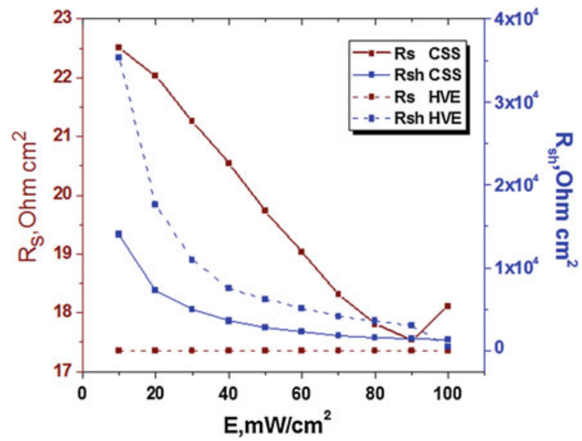

Fig. 5.7 The dependencies R_s = f(E) and R_{sh} = f(E) of the CdS/CdTe photovoltaic devices fabricated by CSS and HVE

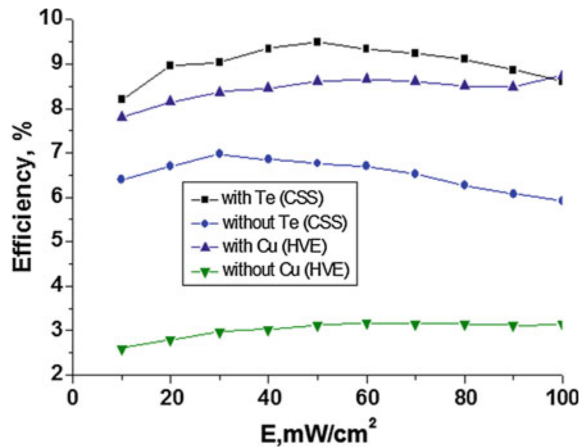

Fig. 5.8 The dependence η = f(E) for CdS/CdTe solar cells fabricated by different methods of deposition

In contrast, R_s for a cell fabricated by HVE varies very little in comparison with the cell fabricated by CSS method. We may conclude that the light-dependent R_{sh} negatively influences the efficiency of our cells.

Temperature dependent measurements often reveal additional information about solar cell operation. Figures 5.9 and 5.10 show the temperature dependence of J-V for two thin film devices. The cell shown in Fig. 9 was fabricated without additional Te layer before the metallic back contact, and the cell with the additional To is illustrated in Fig.10. In both cases, the devices open-circuit voltage increased at reduced temperatures at the expected rate of approximately 2 mV/°C. Also, the current flow becomes more limited as the temperature is reduced. The mechanism for current limitation in the two cases, however, is clearly different. For the devices with Te layer, as noted above, the curves at higher voltages are linear, while without tellurium, they show the characteristic "rollover" behavior, which becomes more pronounced as temperature is reduced. The conclusion is that the Te reduce the back-contact barrier.

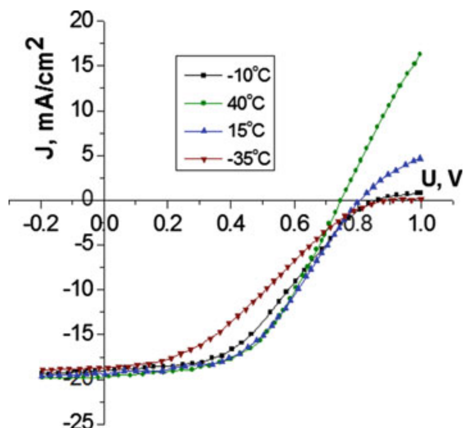

Fig. 5.9 Current-voltage characteristics of the CdS/CdTe device without Te at different measurement temperatures

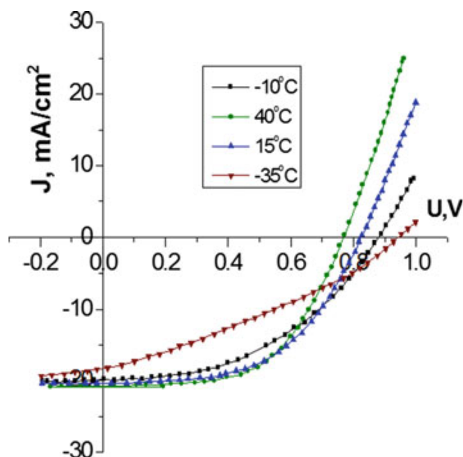

Fig. 5.10 Current-voltage characteristics of the CdS/CdTe device with Te at different measurement temperatures

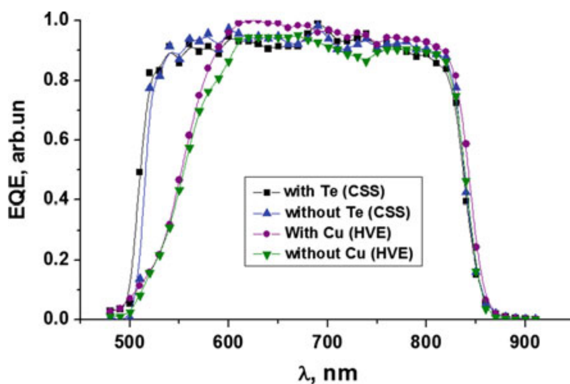

Fig. 5.11 Quantum efficiency of the CdS/CdTe photovoltaic devices fabricated by different methods of deposition

5.6.2 Quantum Efficiency

The external quantum efficiency (EQE) versus wavelength (Fig. 5.11) for the photovoltaic devices fabricated by CSS method with Te and without Te is reasonably good for wavelengths between the band gap of CdS and that of the CdTe. The cells fabricated by HVE with and without Cu have a gradual transition between 500 and 600 nm, which is characteristic for the intermixing between CdTe and CdS thin films. It is well known [42, 43] that the interface consists of $CdTe_{1-y}S_y$/ $CdS_{1-x}Te_x$, where the interfacial values of x and y correspond to the solubility limits in the CdTe-CdS system at the devices processing temperature. These alloys, formed via diffusion across the interface during CdTe deposition and post-deposition treatments, affect photocurrent and junction behavior. Formation of the $CdS_{1-x}Te_x$ alloy on the S-rich side of the junction reduces the band gap and increases absorption, reducing photocurrent in the 500–600 nm range, which we have in the case of cells fabricated by HVE. Comparisons of these cells allow concluding that the cell fabricated by CSS has a high current density because of the larger response in the short wavelengths region.

5.7 Characterization of ZnSe/CdTe Photovoltaic Devices

5.7.1 Morphological and Structural Studies of Glass/SnO_2/ ZnSe Interface

The samples with as-grown ZnSe thin films by close spaced sublimation method obtained at substrate temperatures of 500, 550, 600 and 650 K denoted as (M5.1), (M6.1), (M7.1) and (M8.1), respectively. The samples with ZnSe chloride activated films obtained at substrate temperatures of 500, 550, 600 and 650 K signed as (M5.2), (M6.2), (M7.2) and (M8.2), respectively. The surface of the ZnSe thin films

was analyzed with the SEM scanning electron microscope (SEM) and with the energy dispersive X-ray (EDX). The images were made in the secondary electron (SE) and the backscattered electron modes (BSE). In Fig. 5.12, the SEM images of the ZnSe thin films are illustrated. The SEM images of as-grown films show many round grains on the surface with an inhomogeneous grain size distribution. The films became more crystalline as the substrate temperature increased. The irregular structure of the as-deposited film transformed to a more rounded structure after the annealing. Sample M5.2 with ZnSe after $ZnCl_2$ activation at 400 °C shows many round grains on the surface, and they did not coalesce together. Also, such defects as pinholes are present in the film surfaces which are more visible after chemical activation and annealing.

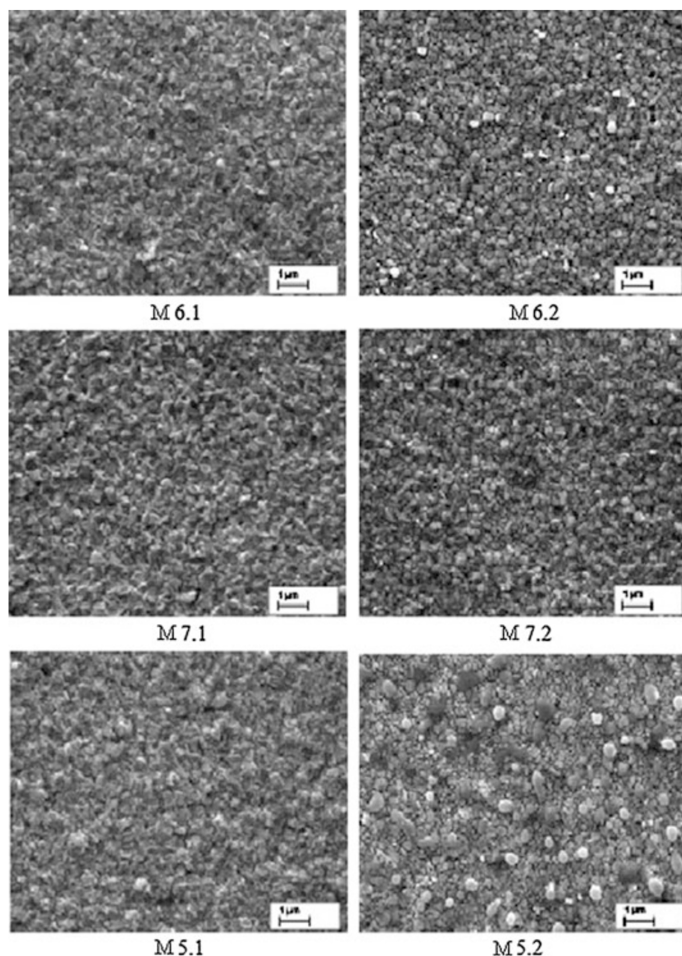

Fig. 5.12 SEM images of ZnSe thin films deposited by close spaced sublimation method: M5.1, M6.1, M7.1—as grown; M5.2, M6.2, M7.2—after $ZnCl_2$ activation and annealing

Fig. 5.13 X-ray diffraction pattern of as-grown ZnSe thin films on SnO_2/glass substrates prepared at different substrate temperatures

The structural characterization of the films was carried out by X-ray diffraction (XRD) measurements using a Rigaku diffractometer with CuKα radiation (λ = 1.5418 Å), at 30 kV, 30 mA. Figure 5.13 shows XRD 2θ scans, between 20° and 80°, for as-deposited ZnSe/SnO_2/glass samples. As seen, the XRD pattern exhibits intensive XRD peaks at 26.52°, 33.79°, 37.85°, 38.84°, 42.55°, 51.64°, 54.51°, 61.69°, 71.04°, 78.44° and 52° from polycrystalline SnO_2 with tetragonal or orthorhombic structures [44] and four peaks with a smaller intensity for the ZnSe phase. The structural parameters for the ZnSe phase are presented in Table 5.3. The X-ray diffraction (XRD) analysis was performed using Rigaku software PDXL. The crystallite size was calculated using the Scherrer's formula from the full-width at half-maximum (FWHM) [45]:

$$D = \frac{k\lambda}{\beta \cos \theta} \tag{5.3}$$

where k is a dimensionless shape factor with a value close to unity, λ is the X-ray wavelength, β—the full-width at half-maximum. The micro strain (ε) was calculated from the formula [45]:

$$\varepsilon = \beta \cos\theta/4 \tag{5.4}$$

where θ is Bragg angle.

The as-deposited ZnSe films are polycrystalline. The XRD patterns of the as-deposited by close spaced sublimation method ZnSe films exhibited reflections corresponding to the cubic phase i.e. 2θ, varies from 2θ = 27.22° to 27.29° with respect to the substrate temperature and corresponding to the (111) plane of the cubic phase. Pradip et al. [46] have reported similar results. Also, the other characteristic diffraction peaks of the diffraction spectra display the cubic phase of ZnSe [44]. However, in all the cases, except M61 sample, the intensity of the (400) peak was high in comparison to the (111) one (see Table 5.3). This indicates a

Table 5.3 Microstructural parameters of CSS method as-deposited ZnSe thin films on SnO_2/glass substrates at different substrate temperatures

No. M51_500 K a = 5.6707 Å	2-theta (deg)	d (ang.)	Height (cps)	β-FWHM (deg)	Size (ang.)	Plane	Strain (%)	Thickness (nm)
1	27.22	3.2728	20940	0.21	413	(111)	0.10	1159.1
2	45.19	2.0046	10239	0.225	399	(220)		
3	53.50	1.7113	15896	0.269	345	(311)		
4	65.76	1.4189	50125	0.238	415	(400)		
2	45.21	2.0036	13237	0.174	517	(220)		
3	53.58	1.7089	28674	0.135	686	(311)		
4	65.703	1.4199	59159	0.225	438	(400)		
No. M61_550 K a = 5.6572 Å	2-theta (deg)	d (ang.)	Height (cps)	β-FWHM (deg)	Size (ang.)	Plane	Strain (%)	
1	27.28	3.2656	29778	0.193	443	(111)	0.16	633.7
2	45.32	1.9991	11313	0.24	375	(220)		
3	53.66	1.7065	20446	0.228	407	(311)		
4	65.93	1.4155	26625	0.282	350	(400)		
2	45.21	2.0036	13237	0.174	517	(220)		
3	53.58	1.7089	28674	0.135	686	(311)		
4	65.703	1.4199	59159	0.225	438	(400)		
No. M71_600 K a = 5.6572 Å	2-theta (deg)	d (ang.)	Height (cps)	β-FWHM (deg)	Size (ang.)	Plane	Strain (%)	
1	27.29	3.2650	15764	0.187	456	(111)	0.23	565.1
2	45.32	1.999	8224	0.288	313	(220)		
3	53.65	1.7070	15964	0.248	375	(311)		
4	65.92	1.4158	28751	0.256	386	(400)		
4	65.703	1.4199	59159	0.225	438	(400)		
No. M81_650 K a = 5.6661 Å	2-theta (deg)	d (ang.)	Height (cps)	β-FWHM (deg)	Size (ang.)	Plane	Strain (%)	
1	27.25	3.2698	17744	0.117	731	(111)	0.13	1008.3
2	45.21	2.0036	13237	0.174	517	(220)		
3	53.58	1.7089	28674	0.135	686	(311)		
4	65.703	1.4199	59159	0.225	438	(400)		

preferential orientation of the micro-crystallites with the (400) direction in the case of the M51, M71 and M81 ZnSe films. The FWHM was found to decrease markedly with film thickness and substrate temperature to 650 K. Such a decrease reflects the increase in the concentration of the lattice imperfections due to the decrease in the internal micro-strain within the films and an increase in the crystallite size. ZnSe thin films of different thicknesses were prepared at different substrate temperatures on glass/SnO_2 substrates. It is observed that the crystallite size increases but the internal strain decreases with the increase of the film thickness and the substrate temperature. The decrease in the strain indicates the formation of higher quality films at higher substrate temperatures. The observed lattice spacing value coincided with the standard JCPDS for cubic ZnSe [44].

The adatom mobility also increases as the substrate temperature increases, which also results in the crystalline size and crystallinity of the films [47]. Good quality polycrystalline thin films of ZnSe can be prepared at a substrate temperature nearer to 650 K, at which the lattice constant 5.6661 Å is found to be closer to the value of bulk ZnSe (5.667 Å) [48].

The X-ray diffraction pattern of $ZnCl_2$ annealed ZnSe thin films at 400 °C in vacuum are shown in Fig. 5.14. The films indicated a cubic ZnSe phase, also. There is no evidence of a new phase formation after $ZnCl_2$ annealing. For all the activated samples, the ZnSe phase presents a slight lattice-parameter decrease compared to the as-grown ones. The change of the lattice constant with the substrate temperatures after $ZnCl_2$ annealing is not very prominent as in the case of films before annealing and suggests that the film grains are stressed. This can be caused by the lattice mismatch and/or differences in the thermal expansion coefficients between the SnO_2 and the glass substrate. The FWHM decreases after $ZnCl_2$ annealing of ZnSe thin films prepared at 500 and 550 K (see Table 5.4). With a further increase of the substrate temperatures, the FWHM increases. It is observed that the crystallite size increases after annealing.

The internal strain increases with the increase of the substrate temperature. The increase of the grain sizes after $ZnCl_2$ annealing indicates an improvement of the ZnSe films crystallinity at 600 and 650 K substrate temperatures in comparison to

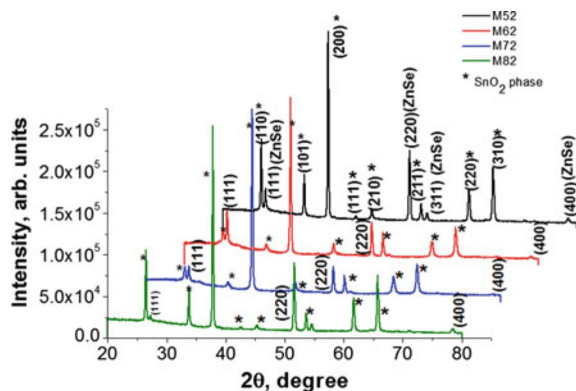

Fig. 5.14 X-ray diffraction pattern of $ZnCl_2$ annealed ZnSe thin films on SnO_2/glass substrates prepared at different substrate temperatures by close spaced sublimation method

Table 5.4 Microstructural parameters of $ZnCl_2$ annealed ZnSe thin films on SnO_2/glass substrates prepared at different substrate temperatures (D-thickness)

No. M52_500 K a = 5.6695 Å	2-theta (deg)	d (ang)	Height (cps)	FWHM (deg)	Size (ang.)	Plane	Strain (%)	D (nm)
1	27.21	3.2741	19263	0.182	470	(111)	0.000000e	1167.1
2	45.21	2.0039	10025	0.216	416	(220)		
3	53.58	1.7088	15797	0.235	396	(311)		
4	65.74	1.4192	57490	0.2351	420	(400)		
No. M62_550 K a = 5.6665 Å	2-theta (deg)	d (ang)	Height (cps)	FWHM (deg)	Size (ang.)	Plane	Strain (%)	D (nm)
1	27.23	3.2721	31484	0.182	470	(111)	0.12	948.9
2	45.24	2.0026	10560	0.236	381	(220)		
3	53.59	1.7086	24892	0.146	637	(311)		
4	65.91	1.4158	29479	0.277	357	(400)		
5	72.63	1.3006	1048	0.36	287	(331)		
No. M72_600 K a = 5.6663 Å	2-theta (deg)	d (ang)	Height (cps)	FWHM (deg)	Size (ang.)	Plane	Strain (%)	D (nm)
1	27.21	3.2735	13142	0.197	434	(111)	0.13	678.9
2	45.26	2.0016	7716	0.276	326	(220)		
3	53.59	1.7086	18775	0.172	540	(311)		
4	65.89	1.4162	29494	0.280	353	(400)		
5	72.67	1.3000	1006	0.44	235	(331)		
No. M82_650 K a = 5.6654 Å	2-theta (deg)	d (ang.)	Height (cps)	FWHM (deg)	Size (ang.)	Plane	Strain (%)	D (nm)
1	27.25	3.2689	4132	0.23	378	(111)	0	1098.2
2	45.22	2.0032	3870	0.30	296	(220)		
3	53.59	1.7084	19302	0.15	620	(311)		
4	65.71	1.4198	61355	0.215	459	(400)		

these films before annealing. The energy dispersive X-ray (EDX) analysis for all CSS method as-deposited and $ZnCl_2$ annealed ZnSe thin films shows very similar characteristics. Both as-deposited and annealed ZnSe films are Zn-deficient and are in good agreement with the results of the paper [49]. This is because the vapor pressure of Se is greater than that of Zn and their sticking coefficients are different. The incorporation of chlorine in the activated ZnSe layers at substrate temperatures is confirmed by the detection of chlorine in a standardless EDX analysis (Fig. 5.15). The chlorine spectrum is very weak because the spectra peaks are almost at the background level.

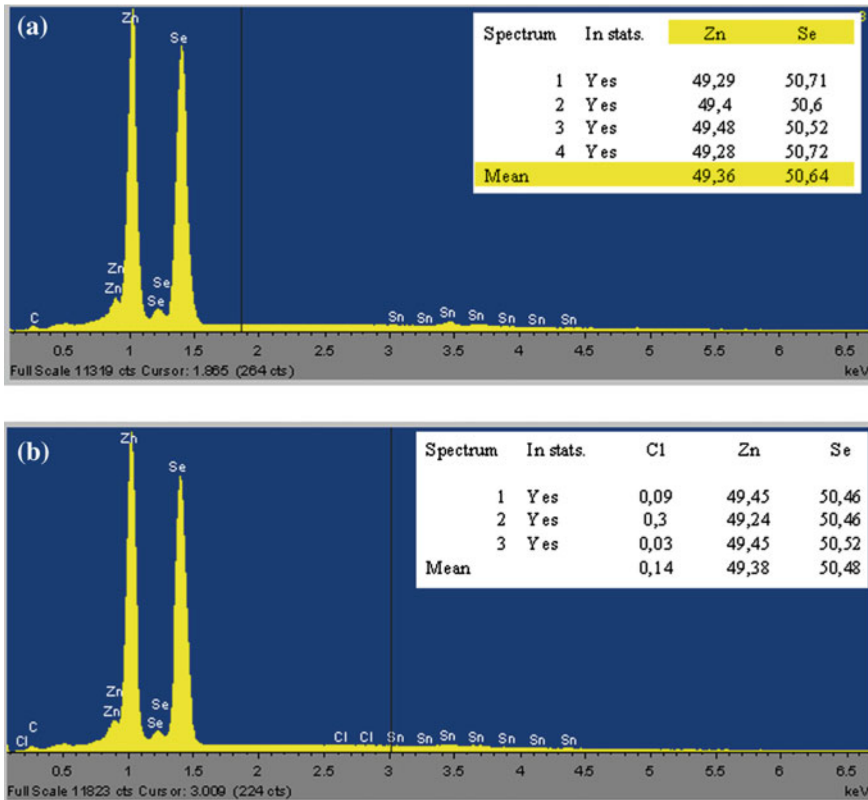

Fig. 5.15 The EDX analyses of as-deposited (**a**) and after $ZnCl_2$ activation (**b**) ZnSe films

5.7.2 Optical Properties of ZnSe Thin Films Deposited on SnO_2/Glass Substrates

The fundamental absorption, which corresponds to the transition from valence band$_2$ to conduction band, can be used to determine the band gap of the material. The relation between *a* and the incident photon energy (hν) can be written as [50]:

$$\alpha = \frac{A(h\nu - E_g)^n}{h\nu} \quad (5.5)$$

where A is a constant, E_g is the band gap of the material and the exponent *n* depends on the type of transition.

The n may have the values 1/2, 2, 3/2 and 3 corresponding to the allowed direct, allowed indirect, forbidden direct and forbidden indirect transitions, respectively. The variation of transmission with wavelength for as-deposited and $ZnCl_2$ annealed ZnSe thin films deposited on SnO_2/glass substrates at different temperatures has been shown in Fig. 5.16. There is a sharp fall of transmittance curve at the band edge, which confirms the crystalline nature of the deposited films. The transmittances in the region of 460–700 nm for $ZnCl_2$ annealed ZnSe films are smaller.

To check the transition type in films the values of n in (5.5) have been calculated by the procedure described elsewhere [50]. The $(\alpha h\nu)^2 = f(h\nu)$ dependencies (Fig. 5.17) for all CSS method ZnSe films are linear at the absorption edge, confirming the direct band gap transition in ZnSe. Extrapolating the straight-line portion of these plots to the $(h\nu)$ axis allows to calculate the band gap (E_g). The optical band gap values for as-deposited ZnSe films prepared at different substrate temperatures ranged between 2.68 eV (0.63 μm) and 2.69 eV (1.16 μm). The

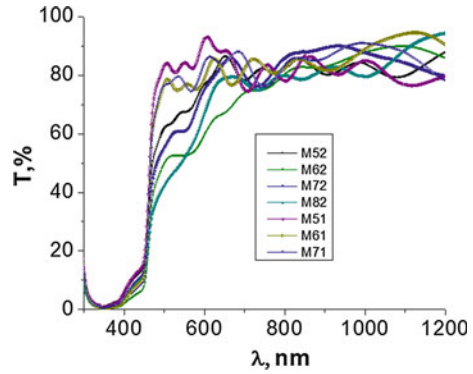

Fig. 5.16 The transmission spectra of as–grown (M5.1, M6.1, M7.1) and $ZnCl_2$ activated and annealed ZnSe thin films at different substrate temperatures

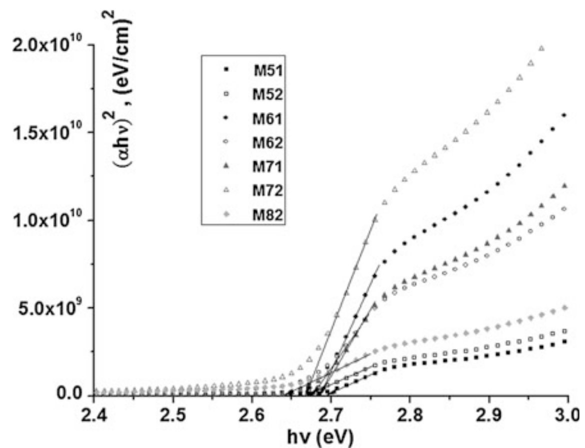

Fig. 5.17 The $(\alpha h\nu)^2 = f(h\nu)$ spectra of as grown (M5.1, M6.1, M7.1) and $ZnCl_2$ activated ZnSe thin films at different substrate temperatures

maximum value of E_g is connected with the very small size of crystallites in films. The thick films have a lower absorption value at the forbidden gap region of the ZnSe films. Thinner films have a high absorption value in the band-band absorption region. This effect may be explained by proposing that thicker films have bigger crystallites (grains) so they are closer to the crystalline ZnSe, but bigger grain sizes give results in larger unfilled inter-granular volumes so the absorption per unit thickness is reduced. One obvious result from the $(\alpha h\nu)^2 = f(h\nu)$ dependence for $ZnCl_2$ activated at 400 °C ZnSe films grown by CSS method at different substrate temperatures is that the energy gap decreases. For example, for sample M51 E_g before annealing is 2.69 eV, after the $ZnCl_2$ activation (sample M52) E_g became 2.66 eV.

The size of crystallites increases with the increase of the substrate temperatures and with $ZnCl_2$ activation. This is confirmed by the XRD analysis (Tables 5.3 and 5.4). This is valid for all ZnSe films regardless of the substrate temperature.

5.7.3 Current-Voltage Characteristics of the ZnSe/CdTe Photovoltaic Devices

Recent effort to improve the efficiency of CdS/CdTe thin film photovoltaic devices is to use wider band gap buffer layers in order to allow more light to reach the junction, consequently improving the short wavelength response of cells and to exclude the formation of a $CdTe_{1-x}S_x$ solid solution near the CdS-CdTe interface with high resistivity and smaller band gap than that for CdS. The study of the dark current-voltage characteristics of several ZnSe/CdTe photovoltaic cells with different thicknesses of ZnSe shows that the direct curves of the I–U characteristic shift in the direction of the current abscissa (Fig. 5.18), which corresponds to an increase in the build-in voltage from 0.46 to 0.52 V. A further increase in the thickness of the ZnSe layer shows that the build-in voltage remains constant. The rectification coefficient of the heterostructure with $d_{ZnSe} = 1.4$ μm calculated at $U_d = U_{rev} = 1$ V is about 2 and increases to 60 with the increasing thickness of the ZnSe film. A further increase in the thickness of the ZnSe layer results in an increase in the series resistance of the heterojunction, which limits the direct current that leads to a decrease in the rectification coefficient. In order to see if there is any effect due to the variation of the substrate temperature of the ZnSe layer deposited by CSS method on photovoltaic parameters we investigated the current-voltage characteristic for photovoltaic devices where the substrate temperature was changed as indicated in Fig. 5.19.

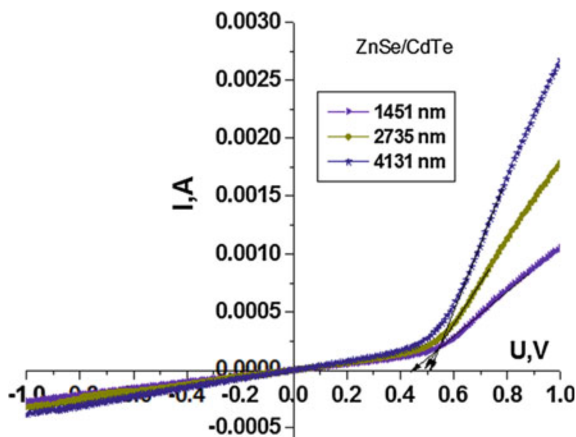

Fig. 5.18 The dark current-voltage characteristics of the ZnSe/CdTe photovoltaic cells with different thicknesses of the ZnSe layer

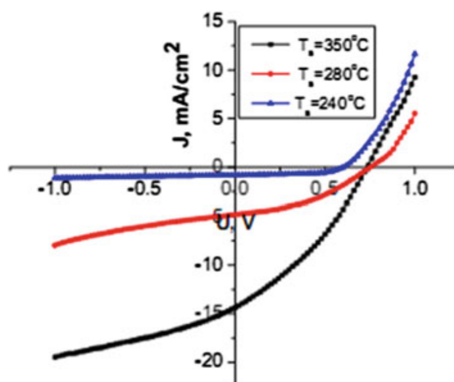

Fig. 5.19 J = f(U) characteristics of the SnO_2/ZnSe/CdTe photovoltaic cells obtained at different substrate temperatures of ZnSe (thickness 2.7 μm); 100 mW/cm^2, 300 K

The photovoltaic parameters of ZnSe/CdTe photovoltaic devices were estimated at the room temperature under the illumination of 100 mW/cm^2 through the wide band gap component ZnSe. The best efficiency of 5.2 % was achieved for the substrate temperature of 350 °C. The open circuit voltage and the current density change significantly with the substrate temperatures. The fill factor is low in general, since series resistance for ZnSe/CdTe is high enough. The photovoltaic characteristics of thin film heterojunction photovoltaic devices with different thicknesses of the ZnSe buffer thin film obtained at T_s = 350 °C are illustrated in Fig. 5.20.

It is obvious that with the ZnSe thin film thickness increase the short circuit current density increases, but the open circuit voltage decreases from 0.75 V at 1.4 and 2.7 μm of ZnSe films to 0.70 V at 4.1 μm of ZnSe thin film thickness. The ZnSe/CdTe photovoltaic cells with an efficiency of 5.5 % were obtained for ZnSe activated and annealed with a thickness of 4.1 μm. Also, the external quantum

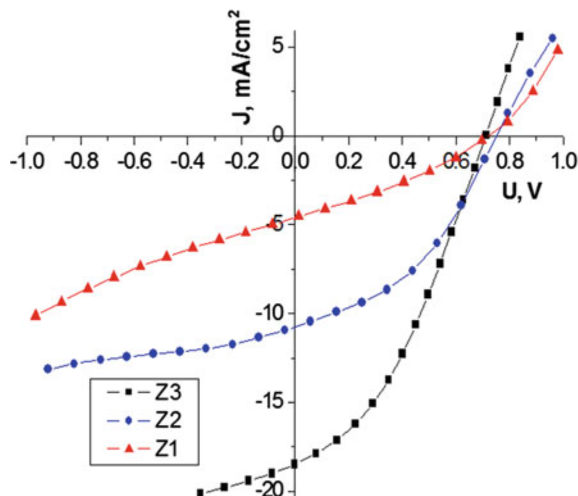

Fig. 5.20 Illuminated current-voltage characteristics of ZnSe/CdTe thin film heterojunction solar cells with different thicknesses of ZnSe: (Z1) 1.4 μm, (Z2) 2.7 μm, and (Z3) 4.1 μm

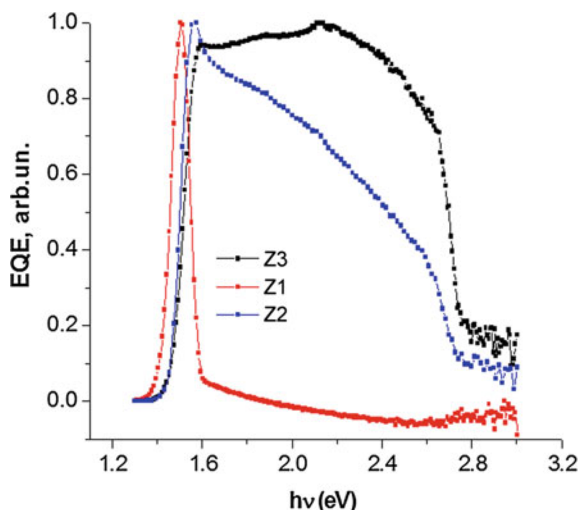

Fig. 5.21 Quantum efficiency of ZnSe/CdTe thin film heterojunction solar cells with different thicknesses of ZnSe

efficiency (Fig. 5.21) for these devices shows that the shape of these characteristics depends on the ZnSe layer thickness. In the case of samples with a thickness of 1.4 μm of ZnSe, almost the whole space charge is situated in CdTe, and the EQE is determined by the electron-hole generation in it. The redistribution of the electron-hole pair generation occurs when increasing the thickness of ZnSe. It is obvious that the contacting materials make an equal contribution to photocurrent if and only if the thickness of the epitaxial layer is on the order of the penetration depth of the contact field. If the thickness is less than the penetration depth, the

major contribution to the EQE is obtained in the sensitivity region of the narrow-band gap material; for the layer thickness higher than the penetration depth of the contact field, it is in the sensitivity region of the wide-band gap material.

5.8 Comparison of CdTe Photovoltaic Devices with Different Buffer Layers

Figure 5.22 compare J-V curves of the best efficiency CdS/CdTe cell with a ZnSe/CdTe cell made by the same technological method, in which the commonly used CdS window is replaced with wider band gap ZnSe to improve the current density.

The photovoltaic parameters for the best ZnSe/CdTe and CdS/CdTe thin film photovoltaic cells are summarized in Table 5.5.

The maximum efficiencies are η = 5.5 % for a cell with a ZnSe buffer and η = 9.6 % for a cell with a CdS buffer. It was found that the ZnSe/CdTe cells present lower values of J_{sc}, and V_{oc}, than those of the CdTe/CdS cells, despite the fact that the SnO_2/ZnSe window allows the transmission of photons in a wider spectral range than the SnO_2/CdS window (Fig. 5.23). This behavior seems to be a consequence of the formation of a better hetero-interface between the CdS and CdTe than between the ZnSe and CdTe thin films. Further studies should be carried out to give a complete explanation of the observed results.

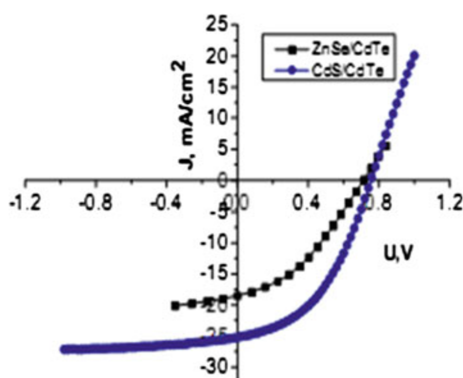

Fig. 5.22 Current-voltage characteristics for the best ZnSe/CdTe and CdS/CdTe thin film photovoltaic devices, 100 mW/cm^2, T = 300 K

Table 5.5 Photovoltaic parameters for the best ZnSe/CdTe and CdS/CdTe thin film photovoltaic devices

Photovoltaic devices	J_{sc} (mA/cm^2)	U_{CD} (V)	FF (%)	η (%)	R_s (Ω cm^2)	R_{sh} (Ω cm^2)
SnO_2/ZnSe/CdTe	20.8	0.63	42	5.5	13.7	256
SnO_2/CdS/CdTe	23.9	0.79	51	9.6	8.4	3769

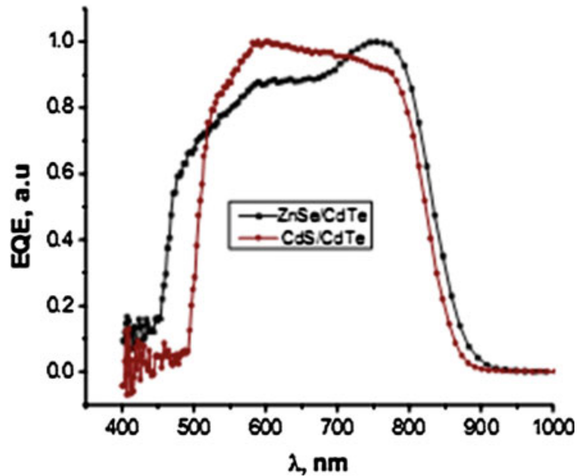

Fig. 5.23 Quantum efficiency for one of the best ZnSe/CdTe and one of the best CdS/CdTe thin film photovoltaic devices

5.9 Photovoltaic Devices Based on TiO_2/CdTe and TiO_2/CdSe Structures

Photovoltaic devices with single-crystal *p*-type CdTe, heterojunctions using stable oxides, such as In_2O_3:Sn (ITO), ZnO, SnO_2 have been investigated. First photovoltaic devices based on *p*-type CdTe single crystals with electron-beam evaporated ITO window layers with $\eta = 10.5$ % were developed by the Stanford group, 1977, with $U_{OC} = 810$ mV, $J_{SC} = 20$ mA/cm^2, and $FF = 65$ % [51]. In 1987, cells made by the reactive deposition of indium oxide, In_2O_3, on *p*-type CdTe single crystals yielded total area efficiencies 13.4 %, with $U_{OC} = 892$ mV, $J_{SC} = 20.1$ mA/cm^2, and $FF = 74.5$ % [52]. In this device, the CdTe crystal had a carrier concentration of 6×10^{15}/cm^3 and the CdTe (111) face were etched in bromine methanol prior to loading into vacuum for In_2O_3 deposition. The U_{OC} of this cell remains the highest ever reported for a CdTe device. The properties of an indium-tin-oxide ITO/CdTe solar cell fabricated by spraying an alcoholic solution of indium chloride and tin chloride on n-type single crystal CdTe were investigated Adeeb et al. [53]. The maximum sensitivity of the ITO/CdTe photovoltaic devices in the visible range attains 0.42 A/W. The efficiency of the solar cells without antireflection coating at AM1 condition is 6.2 %. Photovoltaic devices with ZnO window layers on *p*-type CdTe single crystals yielded poorer junction behavior, with an efficiency <9 % and $U_{OC} = 540$ mV [54]. Using ITO/CdTe, ZnO/CdTe as model systems, we fabricate the TiO_2/CdTe and TiO_2/CdSe photovoltaic devices.

5.9.1 Morphological and Structural Studies of TiO_2 Nanostructured Thin Films

The first set of undoped TiO_2 films was vacuum-annealed at 420 °C for 30 min in the deposition chamber at a pressure of 4.0×10^{-5} mbar and in hydrogen atmosphere at a pressure of 2.0×10^{-3} mbar. A second set of Nb-doped TiO_2 films was annealed at 420 °C for 30 min in hydrogen atmosphere at the same pressure as the first set. We denote the first set of TiO_2 films as MD_2 and the second one as $TiNbO_2$.

The diffraction pattern for the first set of undoped TiO_2 nanostructured films is shown in Fig. 5.24. The various diffraction peaks could be assigned to reflections corresponding to the anatase and rutile phases of TiO_2 (JCPDS data cards 00-021-1272 and 00-21-1276, respectively) for the unannealed and the vacuum-annealed films. For the unannealed TiO_2 film obtained by RF magnetron sputtering the weight percentage of the anatase phase (W_A) is 59.3 % as calculated with the relation [55]

$$W_A = \frac{1}{1 + 1.265 {}^{I_R}/_{I_A}} \tag{5.6}$$

where I_A denotes the intensity of the strongest anatase reflection and I_R is the intensity of the strongest rutile reflection. For the vacuum-annealed film the weight percentage of the anatase phase (W_A) increases to 62 %.The TiO_2 films annealed in H_2 atmosphere exhibit only the anatase phase.

The diffraction spectra of the second set of Nb-doped TiO_2 films are shown in Fig. 5.25. The XRD data show, that the crystallinity is improved when the films are

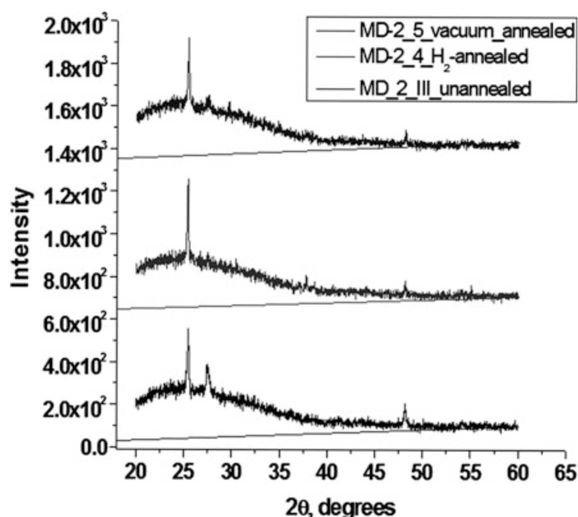

Fig. 5.24 XRD pattern of as-deposited TiO_2 film, vacuum-annealed and annealed in H_2 atmosphere at 420 °C

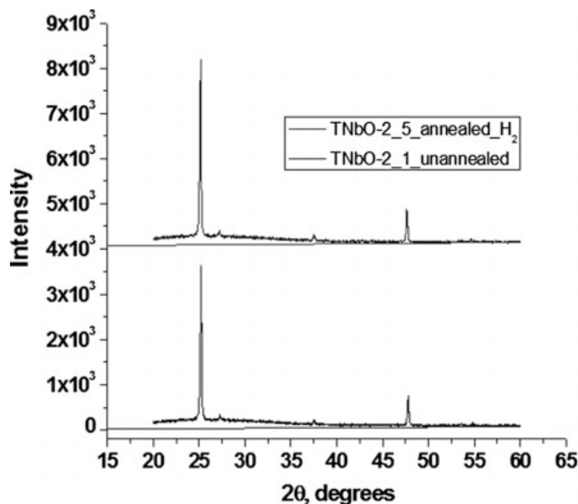

Fig. 5.25 XRD pattern of as-deposited Nb-doped TiO_2 film and annealed in H_2 atmosphere at 420 °C

doped. Annealing at 420 °C in H_2 atmosphere increases the intensity of a diffraction peak at $2\theta = 25.2^o$. No characteristic peaks of Nb_2O_5 were observed in Nb-doped TiO_2 thin films. But it is found that the peak position of (101) anatase plane shifts to a smaller diffracting angle. This may happen because of the exchange of Nb with Ti in the TiO_2 lattice [56] and the formation of the TiNbO phase with different concentrations. This fact was confirmed by the analysis with the TOPAS-Academic V5 software.

The weight percentage of the anatase phase (W_A) is 93 % for annealed Nb-doped TiO_2 film, but for the unannealed it is 96 %. The *a* and *c* lattice parameters of the TiO_2 crystalline cell decrease from ($a = 3.8214$ Å, $c = 9.5868$ Å) to ($a = 3.7842$ Å, $c = 9.5185$ Å), respectively. This is caused by the different concentration of Nb, confirmed below by the XPS analysis (Table 5.6). We suppose that the primary hydrogen annealing mechanism is the chemisorptions of the dissociated hydrogen on the surface of the films. The half width of all the peaks of the Nb-doped and annealed TiO_2 thin films increases. The crystallite size of TiO_2 nanostructured films was calculated by Scherer equation using anatase (101) and (110) rutile phases. As shown in Table 5.7, for TiO_2 samples deposited by RF magnetron sputtering and annealed in H_2 atmosphere at 420 °C the estimated crystallite size for the anatase phase increases for both sets.

Figures 5.26 and 5.27 show the AFM images of Nb-doped TiO_2 films as-deposited by RF magnetron sputtering at room temperature and annealed at 420 °C for 30 min in hydrogen atmosphere. AFM measurements reveal a net discrepancy and indicate an increase of crystallinity of the annealed films. The as-deposited TiO_2 film exhibits a smooth surface with nonuniform grains. After annealing, the surface becomes homogeneous and is composed of many nanocrystalline grains.

Table 5.6 The weight percentage for the Ti2p, Nb3d and O1s lines

Samples	Atom	%	Atom	%
MD_2_4	O1s	38.1	O1s	60.1
(H_2, 420 °C)	C1s	36.7	Ti2p	39.9
	Ti2p	25.3		
MD_2_5	O1s	42.8	O1s	74.0
(unannealed)	C1s	42.2		
	Ti2p3	15.0	Ti2p3	26.0
MD_2_I	O1s	38.1	O1s	61.5
(vacuum, 420 °C)	C1s	38.0		
	Ti2p3	23.8	Ti2p3	38.5
TiNbO_2_1	O1s	41.3	O1s	61.6
(unannealed)	C1s	32.9		
	Ti2p3	21.5	Ti2p3	32.0
	Nb3d	4.3	Nb3d	6.4
TiNbO_2_5	O1s	41.5	O1s	59.8
(H_2, 420 °C)	C1s	30.5		
	Ti2p3	22.1	Ti2p3	31.9
	Nb3d	5.8	Nb3d	8.3

Table 5.7 Structural parameters of TiO_2 nanostructured thin films

Samples	2θ	Int., arb.un	Phase name	d (ang.)	D (nm)
MD_2_5	25.508	601[a]	(101) Anatase	1.7954	51.0
(unannealed)	27.438	283	(110) Rutile	3.3228	44.1
	48.042	170	(200) Anatase	3.1042	
MD_2_1	25.503	556[a]	(101) Anatase	1.7967	51.5
(vacuum, 420 °C)	27.438	386	(110) Rutile	3.3304	
	48.043	204	(200) Anatase	3.1003	
MD_2_4	25.508	636[a]	(101) Anatase	1.7981	88.4
(H_2, 420 °C)	37.793	186	(004) Anatase	2.5118	
	48.048	162	(200) Anatase	3.1064	
TiNbO_2_1	25.192	3643[a]	(101) Anatase	1.8121	47.4
(unannealed)	27.432	246	(110) Rutile	3.3591	
	37.789	156	(004) Anatase	3.7975	
	47.783	749	(200) Anatase	4.1726	
TiNbO_2_5	25.162	4126[a]	(101) Anatase	1.8141	55.2
(H_2, 420 °C)	27.420	226	(110) Rutile	3.3738	
	37.792	207	(004) Anatase	3.7975	
	47.747	827	(200) Anatase	4.1783	

[a]Most intensive X-ray difraction peak

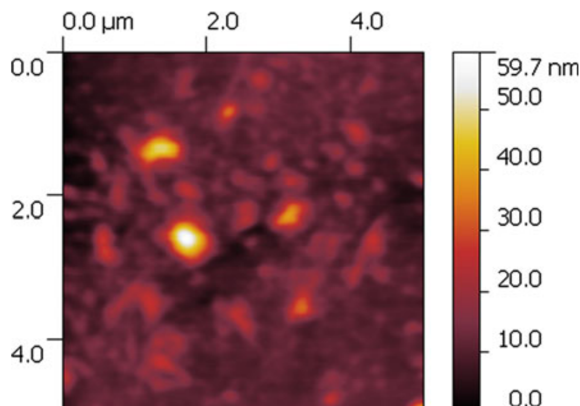

Fig. 5.26 Two-dimensional AFM image of an as-grown Nb-doped TiO_2 thin film

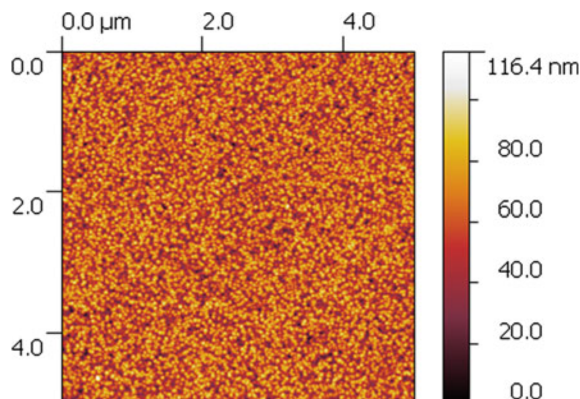

Fig. 5.27 Two-dimensional AFM images of a Nb-doped TiO_2 thin film annealed in H_2 atmosphere at 420 °C

5.9.2 XPS Analysis

Figure 5.28 shows the full range XPS spectra of the first set of TiO_2 films in the whole binding energy region. It can be seen that in the whole region of 0–1200 eV, the characteristic peaks, C1s, O1s and Ti2p are presented. During the XPS experiments for unannealed TiO_2 film the C1s peak position at 284.6 eV is set. For the vacuum and H_2 annealed TiO_2 films the C1s peak position is at 285.7 eV. For the Nb-doped TiO_2 thin films before and after annealing the C1s peak is situated at the same energy. Figure 5.29 shows the results from a fitting procedure with PHI-MATLAB of an XP spectrum of Ti2p for TiO_2 nanostructured thin films of the first set. The experimental contour fits two peaks for all samples. For the unannealed TiO_2 film the spectrum indicates binding energies at 458.5 ± 0.2 eV for Ti2*p*3/2 and 464.3 ± 0.2 eV for Ti 2*p*1/2, respectively, which are very close to the values of the Ti^{4+} valence state of stoichiometric rutile TiO_2 [57, 58]. For the vacuum and H_2 annealed films at 420 °C the binding energies of the Ti2*p* feature shifted toward higher binding energies and are situated at 459.5 ± 0.2 eV for

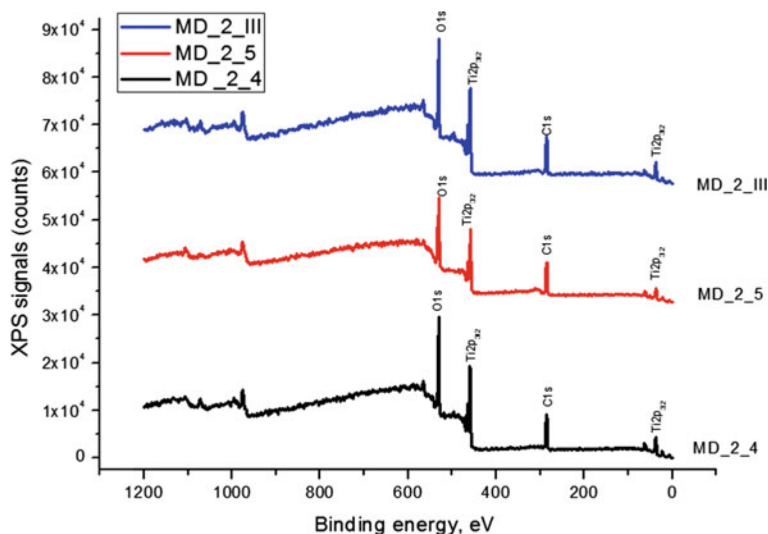

Fig. 5.28 XPS survey scan spectra of an as-deposited TiO_2 film, vacuum-annealed and annealed in H_2 atmosphere at 420 °C

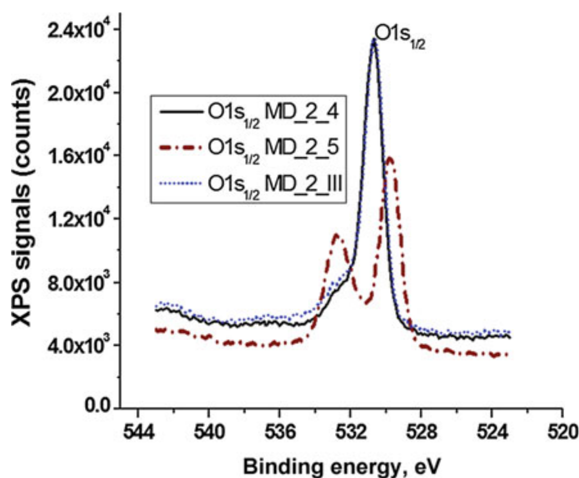

Fig. 5.29 XPS spectra of Ti2p region of an RF magnetron sputtering TiO_2 film, vacuum-annealed and annealed in H_2 atmosphere at 420 °C

Ti2p3/2 and 465.2 ± 0.2 eV for Ti2p1/2 and match well with the reported values for anatase phase [59]. We suppose that this shift may be generated by the reduction of Ti^{4+} ions to Ti^{3+} defect states, which usually are accompanied by a loss of oxygen from the surface of TiO_2.

Liu et al. [60] proposed that the interaction between H_2 and TiO_2 fell into three steps. Firstly, hydrogen interacted physically with the adsorbed oxygen on the surface of TiO_2. Secondly, electrons are transferred from the H atoms to the O atoms in the lattice of TiO_2. Then, the oxygen vacancies are formed when the O atom left

with the H atom in the form of H_2O or OH groups. Thirdly, when the temperature increased to 420 °C, the interaction between H_2 and TiO_2 proceeds more drastically, the electrons are transferred from oxygen vacancies to Ti^{4+} ions, and then Ti^{3+} defect states are formed. Zhang et al. [61] irradiated the TiO_2/Si films by electron beams and found that the number of Ti^{3+} ions increased and Ti^{4+} ions decreased after the irradiation. The weight percentage of the Ti2p and O1s elements in the above mentioned TiO_2 nanostructured thin films are shown in Table 5.7. We can conclude that the Ti^{4+} ions are reduced by both electron donators such as H_2 and lattice oxygen in TiO_2 and the binding energy of 459.5 eV may be attributed in this case to Ti^{3+} defect state of anatase TiO_2 phase according to the XRD analysis. Significant increases in the intensity of the Ti2p peaks for anatase phase are observed, also.

Figure 5.30 shows XPS spectra in O1s region. For the unannealed TiO_2 nanostructured thin film two oxygen chemical species appeared, the lower binding energy species at around 529.7 ± 0.2 eV can be attributed to the basic peak of TiO_2 lattice oxygen (O_{lat}); the other 532. 8 ± 0.2 eV represented the surface weakly bound (or adsorbed) oxygen (OH and molecular O_2 species). The O1s spectrum of the vacuum and H_2 annealed films at 420 °C consists of a main peak with high intensity at about 530.7 ± 0.2 eV and an obvious shoulder located at about 532.9 ± 0.2 eV, indicate that the detected OH group and molecular O_2 may be adsorbed from the surface of the film during annealing. The binding energies of the O1s spectrum of the vacuum and H_2 annealed films shifted toward higher binding energies with the same value 1.0 ± 0.2 eV as for Ti2*p* spectrum of these films.

Figures 5.31, 5.32 and 5.33 present the Nb3d, Ti2p and O1s regions of the RF magnetron sputeriing Nb-doped TiO_2 films and annealed in H_2 atmosphere at 420 ° C. The XPS spectra reveal the Nb3d element. From Table 5.6 we observe that the weight percentage of the Nb3d element is different in TiO_2 films unannealed and annealed in H_2. Therefore, for these samples it is hard to discuss about the influence of the H_2 atmosphere on their structural properties. The Nb3d binding energy for the

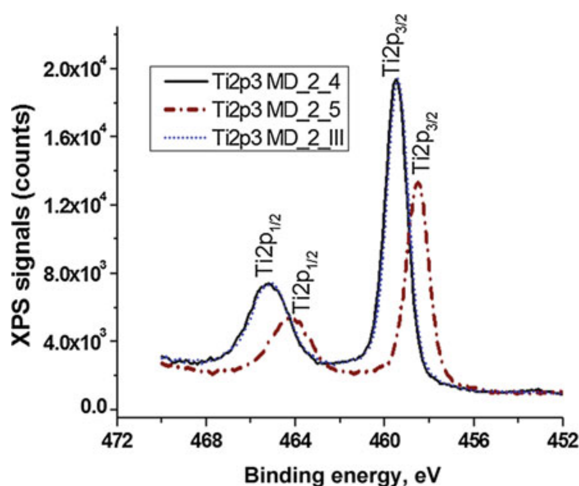

Fig. 5.30 XPS spectra of O1s region of an RF magnetron sputtering TiO_2 film, vacuum-annealed and annealed in H_2

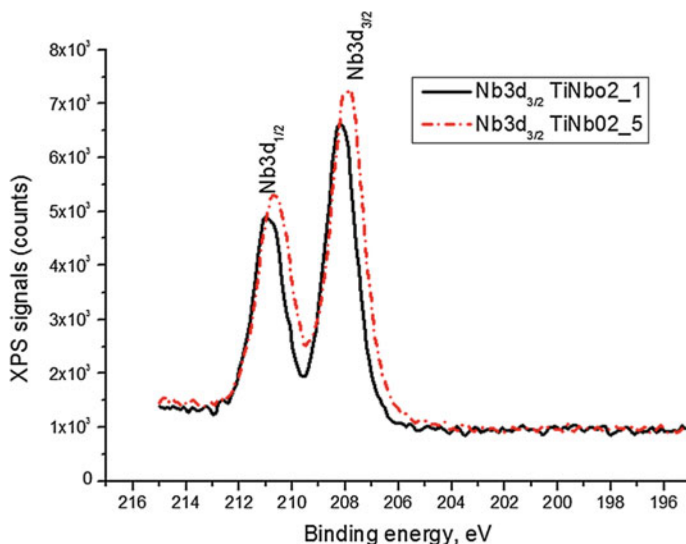

Fig. 5.31 XPS spectra of Nb3d region of an as-deposited Nb-doped TiO_2 nanostructured thin film and H_2 annealed

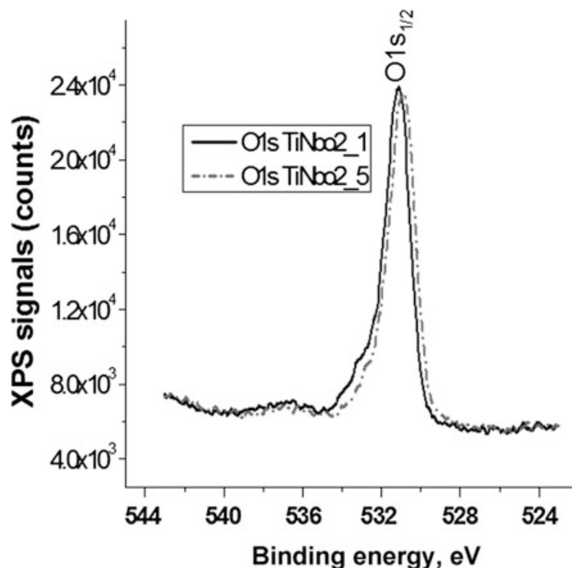

Fig. 5.32 XPS spectra of Ti 2p region of unannealed and annealed Nb-doped TiO_2 films fabricated by RF magnetron sputtering

unannealed Nb-doped TiO_2 film was determined to be 208.2 ± 0.2 eV for Nb3d5/2 and 211.0 ± 0.2 eV for Nb3d3/2, for the annealed one in H_2 atmosphere the binding energy is 207.9 ± 0.2 eV and 210.8 ± 0.2 eV, respectively. We suppose that this shift in these films is caused by the different weight percentage concentration of Nb

Fig. 5.33 XPS spectra of O1s region of unannealed and annealed Nb-doped TiO_2 films fabricated by RF magnetron sputtering

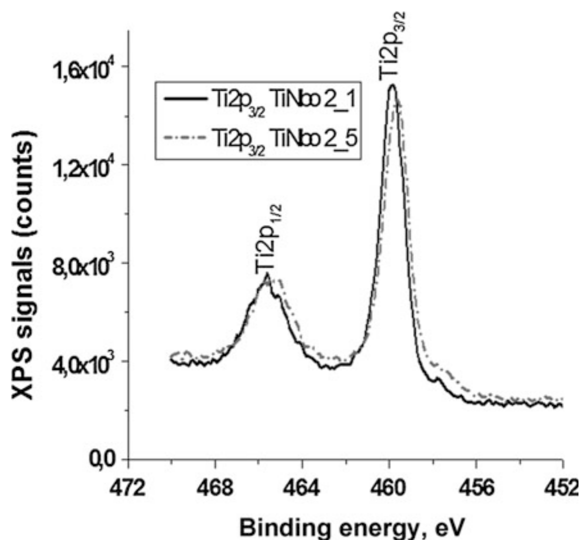

(Table 5.6) and by annealing in H_2 atmosphere at 420 °C. The Ti2p XPS spectra (Fig. 5.32) of unannealed Nb-doped TiO_2 films demonstrate the presence of 459.7 ± 0.2 eV for Ti2p3/2 and 464.9 ± 0.2 eV for Ti 2p1/2. For the film annealed in H_2 atmosphere a slight shift (~0.2 eV) towards higher energy is seen for Ti2p3/2 and (~0.6 eV) for Ti 2p1/2. The position of the Ti 2p3/2 peak (458.8 eV) is close to the value reported for Ti^{3+} states in the anatase phase (458.7 eV) [62].

We think that the H_2 annealing changes the Ti^{3+}/Ti^{4+} ratio in the TiO_2 thin film. Both Ti2p1/2 and Ti2p3/2 binding energies showed a change in Ti^{3+} states and the Ti $^{4+}$ ions as a consequence of the H_2 treatment. A chemical shift of the binding energy of the peaks is known to mean changes in the structure. Since the ionic radii of Nb^{5+} (0.70 A) are larger than the ionic crystal radius of 0.68 A of the titanium we can thus conclude that the Nb is easily built into a lattice, adding electrons. The theoretical calculations of Morgan [63] predict a small-polaronic Ti^{3+}gap state within an Nb-doped TiO_2 thin film. For Nb dopant at these concentrations the defect can be characterized as Nb^{5+} and $Ti^{3+/}Ti^{4+}$ ratio.

The center of the Nb3d3/2 peak corresponds to that of Nb^{5+} oxidation state [64, 65]. Nb^{5+} species, substituting for Ti^{4+} in the crystalline lattice, could be a reason for anatase stabilization. In order to maintain the equilibrium of charges, the extrapositive charge due to Nb^{5+} may be compensated by the creation of an equivalent amount of Ti^{3+} ions [66] or by the presence of vacancies in the cation sites [67].

The XPS spectra of the O1s region of the Nb-doped TiO_2 nanostructured thin films presented in Fig. 5.33 indicate that there is one kind of chemical state. The binding energy of 531.1 ± 0.2 eV for unannealed and 530.8 ± 0.2 eV for annealed Nb-doped TiO_2 films can be attributed to the surface species such as Ti–OH resulting from the chemisorbed water (OH) [68, 69] and to the lattice oxygen (Ti–O), respectively. The shift of the binding energy to small values for the annealed

Nb-doped TiO_2 film can be attributed to the fact that a part of the OH group is adsorbed from the surface because the weight percentage of O atoms is reduced from 61.6 to 59.8 %.

5.9.3 Optical Properties

The optical transmission spectra of the undoped TiO_2 films are shown in Fig. 5.34. The transmission decreases and the position of the interference peaks slightly changes for the annealed TiO_2 thin films. The transmittance of the layers varies between 80 and 90 %, maximum of 90 % being reached for as-deposited TiO_2 fabricated by RF magnetron sputtering. Figure 5.35 shows the variations of transmittance with the wavelength for the Nb-doped TiO_2 thin films. The nearly sharp fall of transmittance curve at the band edge confirms that the doped films have

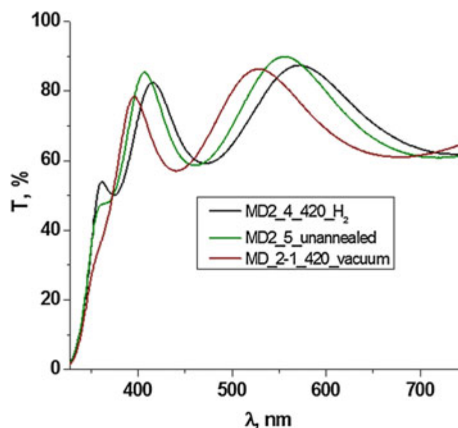

Fig. 5.34 Transmission spectra of undoped TiO_2 nanostructured thin films

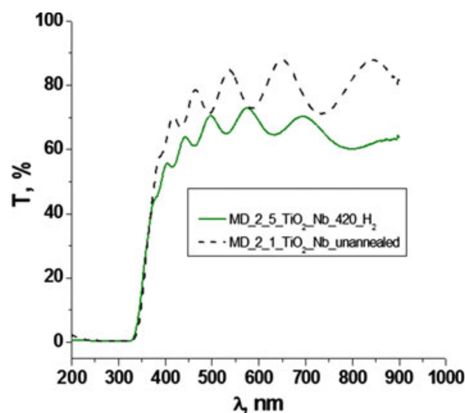

Fig. 5.35 Transmission spectra of the Nb-doped TiO_2 nanostructured thin films

a high crystallinity. The transmission decreases for annealed Nb-doped TiO_2 nastructured thin films in comparison with the undoped films. The optical band gap E_g can be determined from the absorption coefficient α, and it has been investigated by plotting the $(\alpha h\nu)^2 = f(h\nu)$ (for direct allowed transitions) $(\alpha h\nu)^{1/2}$ versus hν (for indirect allowed transitions). In the present study, the best straight line plot extended over most data points is $(\alpha h\nu)^2$ versus hν, as shown in Figs. 5.36 and 5.37. Plots of $(\alpha h\nu)^{1/2}$ versus hν show no linear relationships near the optical absorption edge for TiO_2. The estimated band gap energies of the samples from Figs. 5.36 and 5.37 are summarized in Table 5.8. The maximum band gap reduction was 0.15 eV for Nb-TiO_2 doped unannealed films. H_2 annealing increases the band gap of the Nb-TiO_2 films by 0.03 eV. All band gap values obtained for TiO_2 thin films prepared by RF magnetron sputtering are in good agreement with the reported values from the scientific literature, 3.60–3.75 eV for the direct band gap and 3.05–3.20 eV for the indirect band gap, respectively [70, 71]. Acoording to the XRD analysis TiO_2 is present in two different crystallographic phases. Due to the structural basis the band gap of anatase and rutile is different. The Ti-Ti distances in anatase structure is greater than in rutile, whereas, Ti-O distances are shorter. These

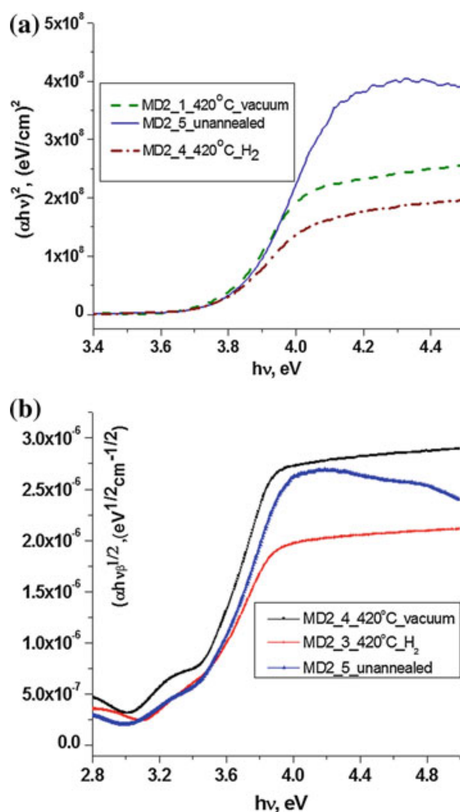

Fig. 5.36 Plots of **a** $(\alpha h\nu)^2 = f(h\nu)$ and **b** $(\alpha h\nu)^{1/2} = f(h\nu)$ of undoped and annealed TiO_2 thin films fabricated by RF magnetron sputtering

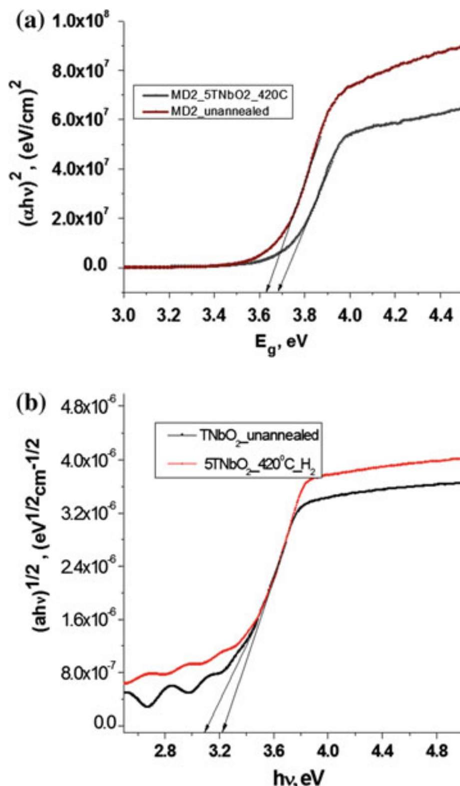

Fig. 5.37 Plots of **a** $(\alpha h\nu)^2 = f(h\nu)$ and **b** $(\alpha h\nu)^{1/2} = f(h\nu)$ of Nb-doped and annealed TiO_2 thin films fabricated by RF magnetron sputtering

Table 5.8 The band gap of the TiO_2 nanostructured thin films

Samples	*d* (nm)	E_g (eV) Direct allowed transitions	*D* (nm)	E_g (eV) Indirect allowed transitions
TNbO2_1_unannealed	321.6	3.63	47.4	3.18
TNbO2_5_ annealed_420 °C_H_2	276.4	3.66	65.2	3.26
MD2_1_vacuum _420 °C	926.7	3.74	51.5	3.26
MD2_4_annealed_420 ° C_H_2	459.6	3.72	88.4	3.27
MD2_5_unannealed	682.1	3.78	51.0	3.29

d -thickness, *D*-grain sizes

structural features change the mass density and lead to different electronic configuration. Rutile phase is 9% higher dense than the anatase presenting more pronounced localization of 3d states and therefore a narrower 3d bands. The O2p and Ti3d hybridization is different in two structure. These different features are responsible for the different band gap.

Table 5.9 Electrical parameters of Nb-TiO_2 films anealed in H_2 atmosphere

T (°C)	ρ (Ω cm)	δ $(\Omega\ cm)^{-1}$	μ (cm^2/V s)	n (cm^{-3})
420	0.74	1.34	3.4	2.4×10^{18}
460	0.4	2.5	0.13	1.7×10^{20}

5.9.4 Electrical Properties

The investigation of the I-U characteristic of the In/TiO_2 indicates that the thermally evaporated indium contact to the TiO_2 nanostructured thin film is a good ohmic contact. TiO_2 thin film possesses *n*-type of conductivity. The main measurements were performed in a constant magnetic field (0.24 T magnetic induction) and with the direct current (DC) stabilized. Each sample was measured for three different values of the current (50 μA–2 mA). For each parameter value the deviation (measurement error) was calculated. These are casual errors and do not include deviations due to the final value of the contact area, i.e. the contacts are not infinitely small points, and the contact area is comparable to the sample surface. The sheet resistance and the Hall effect were measured by the four probe method (Van der Paw method). The measured values of specific electrical conductance and the charge carriers concentration at 295 K for the TiO_2 nanostructured thin films are presented in Table 5.9.

As we can see, the TiO_2 layers treated at lowest temperatures are too resistive to measure with a 4-point probe. With the increase of the annealing temperature, the mobility decreases and the concentration of the charge carriers increases.

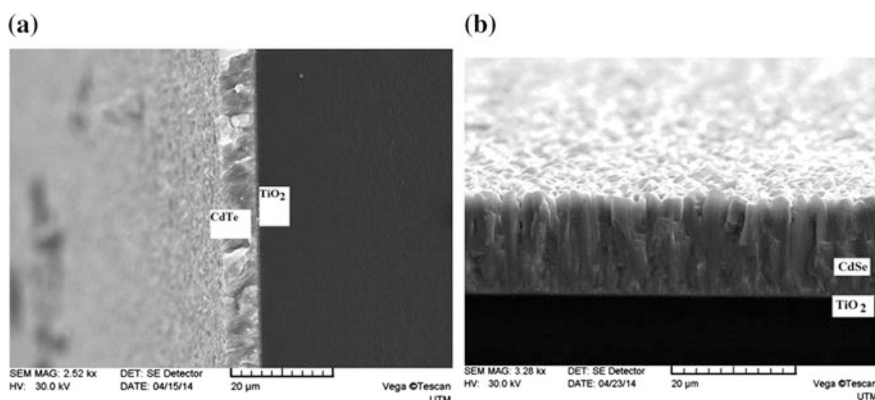

Fig. 5.38 SEM cross-section image of the *n*-TiO_2/*p*-CdTe (**a**) and *n*TiO_2/*n*-CdSe (**b**) heterojunctions

Fig. 5.39 Load J-U characteristics of the TiO_2/CdSe photovoltaic devices under 100 mW/cm^2 illumination, 300 K

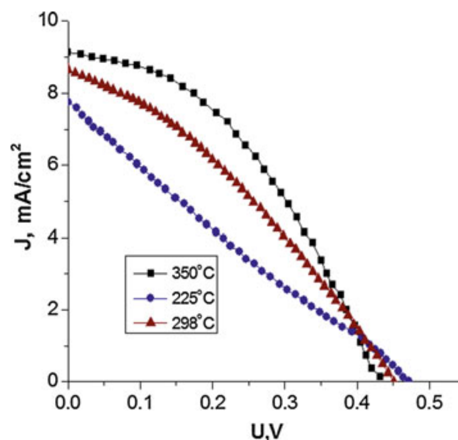

5.10 TiO_2/*p*-CdTe and TiO_2/*n*-CdSe Photovoltaic Devices

The SEM cross-section images of the heterojunctions *n*-TiO_2/*p*-CdTe (a) and *n*TiO_2/*n*-CdSe (b) are shown in Fig. 5.38.

It can be seen that CdTe and CdSe thin films have a columnar morphology. The photovoltaic characteristics of the TiO_2/CdTe and TiO_2/CdSe photovoltaic devices were investigated at 300 K and under the illumination of 100 mW/cm^2 through the wide band gap of the TiO_2. The current-voltage characteristics of TiO_2/CdSe photovoltaic devices obtained at different substrate temperatures of CdSe are illustrated in Fig. 5.39. The photovoltaic parameters are presented in Table 5.10.

The best photovoltaic parameters are achieved for a photovoltaic device with CdSe deposited by CSS method at T_s = 350 °C. As one can see from Table 5.10 the value of the open circuit voltage and the current density for this device reaches 0.43 V and 9.12 mA/cm^2, respectively. The fill factor is low in general for all the devices. As one can see from the shape of the load current-voltage curves the series resistance value is high for all the devices and it is due to the fact that the resistance of Nb-doped and annealed TiO_2 thin films is high enough. The highest efficiency achieved for TiO_2/CdSe photovoltaic devices is 1.63 %.

One of the important factors determining the efficiency of a solar cell is the spectral distribution of the quantum efficiency which accounts for the formation of the drift and diffusion components of the photocurrent, and, ultimately, the short-circuit current density. The location of the long-wave edge of the spectral distribution of the external quantum yield is well correlated with the band gap energy of CdSe (Fig. 5.40).

Table 5.10 Photovoltaic parameters of TiO_2/CdSe photovoltaic devices

T_s (°C)	J_{sc} (mA/cm^2)	U_{oc} (V)	*FF*	η (%)
225	7.74	0.47	0.24	0.87
298	8.73	0.45	0.33	1.26
350	9.12	0.43	0.42	1.63

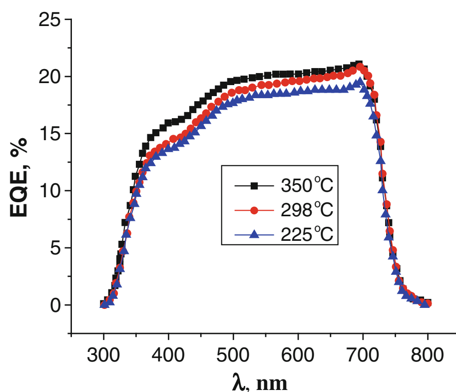

Fig. 5.40 The external quantum efficiency of the TiO_2/CdSe photovoltaic devices at different substrate temperatures of CdSe

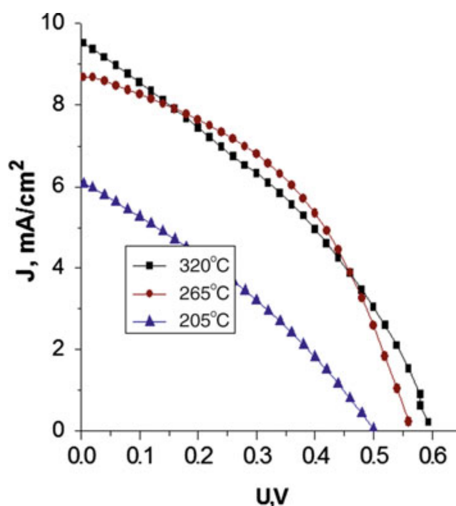

Fig. 5.41 Load current-voltage characteristics of the TiO_2/CdTe photovoltaic devices under 100 mW/cm^2 illumination, 300 K

The load current-voltage characteristics of the illuminated TiO_2/*p*CdTe photovoltaic devices are shown in Fig. 5.41. The photovoltaic parameters depend on the shape of the J-U curve, which is influenced by the substrate temperature of the CdTe thin films. An inspection of Table 5.11, where the photovoltaic parameters are presented, shows that the efficiency of the devices is low because of the low values of the open circuit voltage and the fill factor. Efforts are now in progress to improve the device photovoltaic parameters. The EQE for the TiO_2/*p*CdTe devices, when illuminated through the wide band gap semiconductor (TiO_2), is shown in Fig. 5.42.

As seen from this figure, the EQE extends from 350 to 860 nm, i.e. covers the whole visible range of the solar spectrum and consistent UV-vis region. The quantum efficiency data indicate that with the increase of the substrate temperature of the CdTe thin film fabricated by CSS method the carrier collection is improved.

Table 5.11 Photovoltaic parameters of TiO_2/CdTe photovoltaic devices

T_s (°C)	J_{sc} (mA/cm^2)	U_{oc} (V)	FF	η (%)
205	6.1	0.51	0.27	0.85
265	9.12	0.43	0.42	1.63
320	9.5	0.59	0.36	1.98

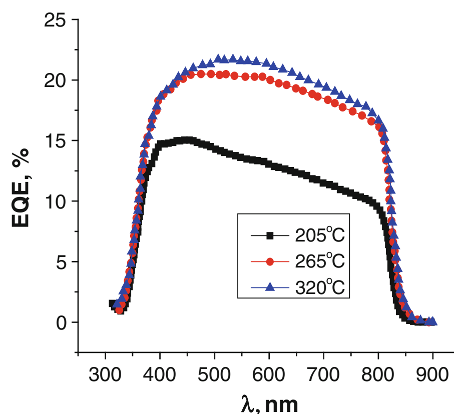

Fig. 5.42 External quantum efficiency of the TiO_2/CdTe photovoltaic devices at different substrate temperatures of CdTe

Both the blue and the red regions of the spectrum show that the charge collection in the device is affected, the red region somewhat more dramatically. This may be caused by the increase of the recombination rate of carriers. We believe that the recombination occurs primarily at the interface and then at the enlarged front and back contacts in these device structures.

5.11 Conclusions

The II–VI compounds have been and continue to be explored for electrical energy generation from solar radiation with the goal to increase efficiency at a low cost. Among A_2B_6 thin-films, CdTe based PV modules have shown remarkable progress with commercialization and become the first PV technology with the price below 1 $/Wp. The comparison of one of the best MSU CdS/CdTe photovoltaic device with a device with a world record efficiency of 18.3 % indicates optical (reflection and absorption), electrical and recombination efficiency losses. Analyses of current-voltage and EQE measurements allow us to identify the efficiency losses in the MSU device. It was shown that the efficiency loss is primarily caused by the fill factor. The FF losses are due to the series resistance R_s, the leakage current, and the ideality factor, the low U_{oc}, voltage dependent current collection, $J_L(U)$ and back contact. The second loss that needs to be addressed occurs for short wavelengths. The absorption losses in SnO_2 and CdS layers decrease J_{SC} to 20–24 %. The world

record efficiency device shown for comparison has partially solved that problem by using a new design at the frontal contact and much thinner CdS thin film. Analysis of J-U and EQE characteristics, of a new ZnSe/CdTe photovoltaic device, shows that the replacement of CdS with ZnSe reduces the frontal CdS absorption loss, but increases the recombination loss due to a larger mismatch ($\sim$12 %) between the lattice parameters of ZnSe and CdTe thin films. The grain boundary interface state density minimizes the efficiency of these devices more than in the case of CdS/CdTe thin film HJs. The losses caused by the light absorption in the 'window' layer of CdS/CdTe solar cells can be reduced by using a material with a wider band gap instead of CdS and ZnSe. Titanium dioxide, one of the best prospective transparent conductive oxides, is widely used in different semiconductor devices due to its high transparency for visible light, large value of the refractive index, controllable specific resistance, good adhesion and high chemical resistance. Also, TiO_2 is environment friendly. The value of the band gap energy of TiO_2 nanostructured thin film varies from 3.15 to 3.6 eV depending on the crystalline structure and deposition technology, that is, about 1 eV larger than that of CdS and ZnSe. This characteristic of TiO_2 allows broadening the spectral region of the photosensitivity of heterojunctions based on CdTe toward the short wavelengths. The photovoltaic devices based on *n*-TiO_2/*p*-CdTe and *n*-TiO_2/*n*-CdSe thin film heterojunctions were fabricated by the deposition of CdTe and CdSe onto TiO_2 thin films prepared by the DC reactive magnetron sputtering technique. Poor efficiency of these devices could be attributed first to the higher sheet resistance of TiO_2 films and, secondly, to the relatively high concentration of mismatch dislocations at the TiO_2/CdTe and TiO_2/CdSe heterojunction interfaces. Note that the TiO_2/CdTe and TiO_2/CdSe heterojunctions were fabricated without the application of additional treatments. It is evident that the controllable change of technological parameters of the TiO_2 thin films deposition, the modification of the CdTe surface, the annealing of the heterojunctions in different atmospheres, as well as the introduction of additional intermediate layers can reduce the surface states concentration at the TiO_2/CdTe and TiO_2/CdSe interfaces and enhance the efficiency of the photovoltaic conversion. Finally, for the MSU CdTe photovoltaic devices to be competitive with the world record technologies, the problems related to contact resistivity, increasing the *p*-type carrier concentration in CdTe, identification and reduction of the density of limiting intragrain defect states, defining and overcoming performance limitations related to back-contact formation on CdTe must be solved.

Acknowledgments The author would like to thank Dr. L. Ghimpu, PhD student N. Spalatu, MPs P. Dumitriu for their help in developing the photovoltaic devices fabrication technology based on A_2B_6 compounds. Also, I am thankful to all the scientists from the Department of Physics and Engineering at MSU for their support and helpful discussions. Many thanks to the team led by prof. D. Luca from Physics Department at "Al. Cuza" University, Romania, for supplying us TiO_2 thin films, for their support with XPS and XRD measurements. I am also grateful to those numerous worldwide scientists and engineers whose data have been included in this overview. This research was supported by the EU 7th Framework Program PEOPLE International Research Staff Exchange Scheme project GA-2008, no. 230861 and by the Bilateral grant no. 13.820.15.19/RoA.

References

1. A.D. Upadhyaya, V. Yelundur, A. Rohatgi, High efficiency mono-crystalline solar cells with simple manufacturable technology, in *Proceedings of 21st European Photovoltaic Solar Energy Conference and Exhibition*, Dresden, Germany, 4–8 Sept 2006
2. W. Heywang, K.H. Zaininger, Silicon: the semiconductor material, in *Silicon: Evolution and Future of a Technology*, ed. by P. Siffert, E.F. Krimmel (Springer, New York, 2004
3. M. Taguchi, *Solar Bus.* Unit (Sanyo Electr. Co., Ltd., Kobe, Japan) (A. Yano, S. Tohoda, K. Matsuyama, IEEE J. Photovolt. **4**(1), 96–99)
4. B.M. Kayes, H. Nie, R. Twist, S.G. Spruytte, F. Reinhardt, I.G. Kizilyalli, G.S. Higashi, in *Proceedings of the 37th IEEE Photovoltaic Specialists Conference*, Seattle, Washington, USA (2011)
5. M.A. Green, K. Emery, Y. Hishikawa, W. Warta, E.D. Dunlop, Progr. Photovolt. **21**, 827S (2013) (R. Wenham, M.A. Green, M.E. Watt, R. Corkish, *Applied Photovoltaics* (Earthscan, 2007), Chap. 2
6. S.R. Wenham, M.A. Green, M.E. Watt, R. Corkish, *Applied Photovoltaics* (Earthscan, 2007), Chap. 2
7. A. Morales-Vilches, C. Voz, M. Colina, G. Lopez, I. Martin, A. Orpella, J. Puigdollers, M. Garcia, R. Alcubilla, *Electron Devices (CDE), 2013 Spanish Conference* 12–14 Feb 2013, pp. 345–348
8. R.W. Collins, et al., Evolution of microstructure and phase in amorphous, protocrystalline, and microcrystalline silicon studied by real time spectroscopic ellipsometry. Solar Energy Mater. Solar Cells **78**(1–4), 143–180 (2003)
9. M. Gloeckler, I. Sankin, Z. Zhao, CdTe solar cells at the threshold to 20 %. IEEE J. Photovolt. **3**(4), 1389–1393 (2013)
10. P. Jackson, D. Hariskos, E. Lotter, S. Paetel, R. Wuerz, R. Menner, W. Wischmann, M. Powalla, New world record efficiency for Cu(In, Ga)Se2 thin-film solar cells beyond 20 %. Prog. Photovolt: Res. Appl. **19**, 894–897 (2011)
11. X. Wu, High-efficiency polycrystalline CdTe thin-film solar cells. Sol. Energy **77**(6), 803–814 (2004)
12. D.L. Baltzner, A. Romeo, H. Zogg, R. Wendt, A.N. Tiwari, Development of efficient and stable back contacts on CdTe/CdS solar cells. Thin Solid Films **387**(1–2), 151–154 (2001)
13. J. Loferski, J. Appl. Phys. **27**, 777–784 (1956)
14. E. Adirovich, Y. Yuabov, D. Yugadaev, Sov. Phys. Semicond. **3**, 61–65 (1969)
15. D. Bonnet, H. Rabenhorst, *Conference on Record on 9th IEEE Photovoltaic Specialist Conference*, pp. 129–132 (1972)
16. J.P. Enrıquez, X. Mathew, G.P. Hernández, U. Pal, D.R. Maganã, D.R. Acosta, R. Guardian, J. A. Toledo, G. Contreras Puente, J.A. Chavez Carvayar, CdTe/CdS solar cells on flexible molybdenum substrates. Solar Energy Mater. Solar Cells **82**, 307–314 (2004)
17. I. Matulionis, H. Sijin, J.A. Drayton, K.J. Price, A.D. Compaan, Cadmium telluride solar cells on molybdenum substrates, in *Proceedings of the Materials Research Society Symposium on II–VI Compound Semiconductor Photovoltaic Materials,* Warrendale, PA, USA, vol. 668, H8.23 (2001), pp. 1–6
18. P.S. Vijay, C.M. John, G.B. Lush, W. Wang, X. Wang, G.W. Thompson, E. Clark, Thin film CdTe–CdS heterojunction solar cells on lightweight metal substrates. Solar Energy Mater. Solar Cells **59**, 145–161 (1999)
19. X. Mathew, J.P. Enriquez, A. Romeo, A.N. Tiwari, CdTe/CdS solar cells on flexible substrates. Solar Energy **77**, 831–838 (2004)
20. Y.S. Tyan, E.A. Perez-Albuerne, Efficient thin-film CdS/CdTe solar cells, in *Proceedings of the 16th IEEE Photovoltaic Specialists Conference*, pp. 794–800, New York, NY, USA (1982)
21. B.M. Basol, Electrodeposited CdTe and HgCdTe solar cells. Solar Cells **23**, 69–88 (1988)

22. T.L. Chu, Thin film cadmium telluride solar cells by two chemical vapour deposition techniques. Solar Cells **23**, 31–48 (1988)
23. K.W. Mitchell, C. Eberspacher, F. Cohen, J. Avery, W. Duran, W. Bottenberg, Progress towards high efficiency thin film CdTe solar cells. Solar Cells **23**, 49–57 (1988)
24. C. Ferekides, J. Britt, Y. Ma, L. Killian, High efficiency CdTe solar cells by close spaced sublimation, in *Proceedings of the 23rd IEEE Photovoltaic Specialists Conference*, pp. 389–393, New York, NY, USA, May 1993
25. X. Wu, J.C. Keane, R.G. Dhere, C. DeHart, D.S. Albin, A. Duda, T.A. Gessert, S. Asher, D.H. Levi, P. Sheldon, 16.5 %-efficient CdS/CdTe polycrystalline thin-film solar cells, in *Proceedings of the 17th European PVSEC* (2001), pp. 995–1000
26. D.A. Cusano, CdTe solar cells and PV heterojunctions in II-VI Compounds. Solid State Electron. **6**(3), 217 (1963)
27. P. Meyers, C. Liu, T. Frey, U.S. Patent 4,710,589 (1987)
28. J.F. Nolan, P.V. Meyers, Fabrication of stable large-area thin-film CdTe photovoltaic modules. Annual subcontracting report, NREL/TP-413–5740 (1993)
29. T. Aramoto, M. Tsuji, T. Yamamoto, T. Nishio, P. Veluchamy, H. Higuchi, S. Kumazawa, J. Shibutani, S. Nakajima, Y. Nishiyama, T. Arita, A. Hanafusa, T. Hibino, K. Omura, Highly efficient large area thin film CdS/CdTe sub-module solar cells, in *Proceedings of 28th IEEE Photovoltiac Specialist Conference*, pp. 436–439
30. D. Bonnet, Manufacturing of CSS CdTe solar cells. Thin Solid Films **361–362**, 547 (2000)
31. M. Gloeckler, I. Sankin, Z. Zhao, CdTe solar cells at the threshold to 20 % efficiency, in *Proceedings of 39th IEEE Photovoltiac Specialist Conference*, 2013, pp. 436–439
32. M.A. Green, K. Emery, D.L. King, S. Igari, W. Warta, Solar cell efficiency tables (Version 18). Progr. Photovolt. Res. Appl. **9**, 287–293 (2001)
33. M.A. Green, K. Emery, Y. Hishikawa, W. Warta, E.D. Dunlop, Solar cell efficiency tables (version 40). Prog. Photovolt: Res. Appl. **20**, 606–614 (2012)
34. M.A. Green, K. Emery, Y. Hishikawa, W. Warta, E.D. Dunlop, Solar cell efficiency tables (version 41). Prog. Photovolt: Res. Appl. **21**, 1–11 (2013)
35. Press Release, First Solar, 22 April 2013, [Online]
36. A. Kanevce, D.H. Levi, D. Kuciauskas, The role of drift, diffusion, and recombination in time-resolved photoluminescence of CdTe solar cells determined through numerical simulation. Progr. Photovolt. (2013)
37. S.H. Demtsu, J.R. Sites, in *Proceedings of the 30th IEEE Photovoltaic Specialist Conference*, pp. 744–747, 2005
38. P. Gashin, T. Potlog, L. Ghimpu, T. Potlog, L. Ghimpu, P. Gashin, A. Pudov, T. Nagle, Sites. J Solar Energy Mater. Solar Cells **80**, 327–334 (2003)
39. Yu.Z. Bubnov , M.S. Lurie , F.G. Starh , G.A. Filaretov. The vacuum deposition of films in the quasi-closed volume. M. , Sov . radio,(1975)
40. T. Potlog, N. Spalatu, N. Maticiuc, J. Hiie, A. Mere, V. Valdna, V. Mikli Structural reproductibility of CdTe thin films deposited on different substrates by close space sublimation method. Phys. Status Solidi (A) **209**(2), 272–276 (2012)
41. D. Batzner, A. Romeo, H. Zogg, R. Wendt, A. Tiwari, Thin Solid Films **151**, 387 (2001)
42. E. Brian, McCandless, H. Gregory, D. Hanket, J. Garth, R.W. Birkmire, J. Vac. Sci. Technol. A **20**(4), 1462–1467 (2002)
43. S. Wei, S. Zhang, A. Zunger, J. Appl. Phys. **87**, 1304–1311 (2000)
44. JCPDS X-ray powder files data (Data file 05–0522)
45. G. Gordillo, E. Romero, C. Quinones, Study of structural properties of Zn(S,Se) thin films deposited by evaporation, in *19th European Photovoltaic Solar Energy Conference* pp. 1780–1783 (2004)
46. Pradip K. R. Kalita, B. K. Sarma and H. L. Das. Structural characterization of vacuum evaporated ZnSe thin films. Bull. Mater. Sci., Vol. 23, No. 4, August, pp. 313–317 (2000)
47. R.B. Kale, C.D. Lokhande, Influence of air annealing on the structural, morphological, optical and electrical properties of chemically deposited ZnSe thin films. Appl. Surf. Sci. **252**(4), 929–938 (2005)

48. H. Morkoç, S. Strite, G.B. Gao, M.E. Lin, B. Sverdlov, M. Burns, Large-band-gap SiC, III-V nitride, and II-VI ZnSe-based semiconductor device technologies. J. Appl. Phys. **76**, 1363–1398 (1994)
49. G. Hodes, in *Physical Electrochemistry: Principles, Methods and Applications*, ed. by I. Rubinstein (Marcel Dekker Inc., New York, 1995), pp. 515–554
50. G. Perna, M. Lastella, M. Ambrico, V. Capozzi, Temperature dependence of the optical properties of ZnSe films deposited on quartz substrate. Appl. Phys. A **83**, 127–130 (2006)
51. K. Mitchell, A. Fahrenbruch, R. Bube, J. Appl. Phys. **48**, 829–830 (1977)
52. T. Nakazawa, K. Takamizawa, K. Ito, Appl. Phys. Lett. **50**, 279–280 (1987)
53. N. Adeeb, I. Kretsu, D. Sherban, C. Sushkevich, A. Simashkevich, Spray deposited ITO/CdTe solar cells. Solar Energy Mater. **15**(1), 9–19 (1987). ISSN 0927-0248
54. J. Aranovich, D. Golmayo, A. Fahrenbruch, R. Bube, J. Appl. Phys. **51**, 4260–4265 (1980)
55. JCPDS X-ray powder file data (Data file 05–0522)
56. R. Sharma, M. Bhatnagar, Sens. Actuators B **56**(3), 215–219 (1999)
57. H.S. Kim, S.H.Kang, Effect of hydrogen treatment on anatase TiO_2 nanotube arrays for photoelectrochemical water splitting. Bull. Korean Chem. Soc. **34**(7), 2067–2072 (2013)
58. H. Bae, S.H. Park, A. Nakamura, K. Koike, K. Fujii, H.-J. Park, H.-J. Lee, T.-S. Oh, J.-S. Ha, The effect of rapid temperature annealing with N_2 and H_2 on photoelectrochemical properties of u-TiO_2. J. Electrochem. Soc. **160**(11), H800–H802. http://jes.ecsdl.org/content/160/11/H800.abstract-fn-2
59. C.D. Wagner, W.M. Riggs, L.E. Davis, J.F. Moulder, G.E. Muilenberg, *Handbook of X-ray Photoelectron Spectroscopy* (Perkin Elmer Corp. Publishers, Eden Prairie, MN, 1979), p. 68
60. J. Liu, S. Xu, L. Liu, D.D. Sun, The size and dispersion effect of modified graphene oxide sheets on the photocatalytic H_2 generation activity of TiO_2 nanorods. Carbon **60**, 445–452. doi:10.1016/j.carbon.2013.04.059
61. J. Zhang, Y. Wang, Z. Jin, Z. Wu, Z. Zhang, Visible-light photocatalytic behavior of two different N-doped TiO_2. Appl. Surf. Sci. **254**, 4462–4466 (2008)
62. M.Z. Atashbar, H.T. Sun, B. Gong, W. Wlodarski, R. Lamb, XPS study of Nb-doped oxygen sensing TiO_2 thin films prepared by sol-gel method. Thin Solid Films **326**(1–2), 238–244 (1998)
63. B.J. Morgan, D.O. Scanlon, G.W. Watson, J. Mater. Chem. 19, 5175–5178 (2009)
64. J.F. Moulder, W.F. Stickle, P.E. Sool, K.D. Bomben, *Handbook of X-Ray Photoelectron Spectroscopy* (Perkin-Elmer Corporation, Eden Prairie, Minn, USA, 1999)
65. M. Valigi, D. Cordischi, G. Minelli, P. Natale, P. Porta, A structural, thermogravimetric, magnetic, electron spin resonance, and optical reflectance study of the NbO_xTiO_2 system. J. Solid State Chem. **77**(2), 255–263 (1988)
66. M. Sacerdoti, M.C. Dalconi, M.C. Carotta et al., XAS investigation of tantalum and niobium in nanostructured TiO_2 anatase. J. Solid State Chem. **177**(6), 1781–1788 (2004)
67. M. Park, T.E. Mitchell, A.H. Heuer, J. Am. Ceram. Soc. **58**, 43–47 (1975)
68. J.C. Colmenares, M.A. Aramendıa, A. Marinas, J.M. Marinas, F.J. Urbano, Appl. Catal. A: Gen. **306**, 120–127 (2006)
69. S.P. Kowalczyk, F.R. McFeely, L. Ley, V.T. Gritsyna, D.A. Shirley, Sol. St. Commun. **23**, 161 (1977)
70. B. Liu, L. Wen, X. Zhao. The photoluminescence spectroscopic study of anatase TiO_2 prepared by magnetron sputtering. Materials Chemistry and Physics, V. 106, Iss. 2–3, pp. 350–353 (2007)
71. F.A. Jenkins, H.E. White, *Fundamentals of Optics*, 4th edn. (New York, McGraw Hill, 1976)